

COSMOGLOBE DR2. I. Global Bayesian analysis of COBE-DIRBE

D. J. Watts^{1*}, M. Galloway¹, E. Gjerløw¹, M. San¹, R. Aurlien¹, A. Basyrov¹, M. Brilenkov¹, H. K. Eriksen¹, U. Fuskeland¹, L. T. Hergt²,
 D. Herman¹, H. T. Ihle¹, J. G. S. Lunde¹, S. K. Næss¹, N.-O. Stutzer¹, H. Thommesen¹, and I. K. Wehus¹

¹ Institute of Theoretical Astrophysics, University of Oslo, Blindern, Oslo, Norway

² Department of Physics and Astronomy, University of British Columbia, 6224 Agricultural Road, Vancouver BC, V6T1Z1, Canada

August 21, 2024

ABSTRACT

We present the first global Bayesian analysis of the time-ordered Diffuse Infrared Background Experiment (DIRBE) data within the COSMOGLOBE framework, building on the same methodology that has previously been successfully applied to *Planck* LFI and *WMAP*. These data are analyzed jointly with *COBE*-FIRAS, *Gaia*, *Planck* HFI, and WISE observations, which allows for a more accurate instrumental and astrophysical characterization than possible through single-experiment analysis only. This paper provides an overview of the analysis pipeline and main results, and we present and characterize a new set of zodiacal light subtracted mission average (ZSMA) DIRBE maps spanning the wavelength range between 1.25 and 240 μm . A key novel aspect of this processing is the characterization and removal of excess radiation between 4.9 and 60 μm that appears static in solar-centric coordinates. The new DR2 ZSMA maps have several notable advantages with respect to the previously available maps, including 1) lower zodiacal light (and possibly straylight) residuals; 2) better determined zero-levels; 3) natively HEALPix tessellated maps with a 7' pixel size; 4) nearly white noise at pixel scales; and 5) a more complete and accurate noise characterization established through the combination of Markov Chain Monte Carlo samples and half-mission maps. In addition, because the model has been simultaneously fitted with both DIRBE and HFI data, this is the first consistent unification of the infrared and CMB wavelength ranges into one global sky model covering 100 GHz to 1 μm . However, we do note that even though the new maps are improved with respect to the official maps, and should be preferred for most future analyses that require DIRBE sky maps, they still exhibit non-negligible zodiacal light residuals between 12 and 60 μm . Further improvements should be made through joint analysis with complementary infrared experiments such as IRAS, AKARI, WISE and SPHEREx, and thereby release the full combined potential of all these powerful infrared observatories.

Key words. ISM: general - Zodiacal dust, Interplanetary medium - Cosmology: observations, diffuse radiation - Galaxy: general

Contents

1	Introduction	1	7	Excess radiation model	18
2	Global Bayesian modelling of the infrared sky	3	7.1	Characterization	18
2.1	Data model and posterior distribution	3	7.2	Mitigation through masking and subtraction	20
2.2	Gibbs sampling with Commander3	6	7.3	Zero-level determination	20
3	Diffuse Infrared Background Experiment	7	8	Frequency maps	24
3.1	The DIRBE instrument	7	8.1	ZSMA frequency maps	24
3.2	Pointing, beam and bandpass response	8	8.2	Angular power spectra	26
3.3	Data selection and masking	8	8.3	Comparison with K98	27
4	Ancillary data sets	9	9	Conclusions	29
4.1	<i>Planck</i> HFI	9	1. Introduction		
4.2	<i>Gaia</i> and WISE	9	The astrophysical sky contains a wealth of information about our own Solar System, the Milky Way, and the high-frequency universe in the infrared wavelength regime from roughly 1 to 1000 μm (e.g., Johnson 1966; Soifer et al. 1987; Gardner et al. 2006). These wavelengths have therefore been the target of many ground-breaking experiments during the last five decades, most of which have been satellite-based due to the high opacity of the Earth's atmosphere. The first transformational observations were made by the NASA-led Infrared Astronomical Satellite (IRAS, Neugebauer et al. 1984), which observed the sky for ten months in 1983, covering four wavelength bands from 12 to 100 μm . IRAS revealed for the first time the intricate nature of thermal dust emission both in the Solar System and the Milky Way.		
4.3	<i>COBE</i> -FIRAS	10			
4.4	Mask definitions	10			
5	Markov chains, burn-in and convergence	10			
6	Noise estimation and goodness of fit	12			
6.1	Instrumental noise	12			
6.2	Goodness of fit	17			

* Corresponding author: D. Watts; duncan.watts@astro.uio.no

arXiv:2408.10952v1 [astro-ph.CO] 20 Aug 2024

IRAS was quickly followed by another NASA-led satellite experiment called Cosmic Background Explorer (*COBE*, [Boggess et al. 1992](#)), which launched in 1989 and carried three instruments. One of these was the Diffuse Infrared Background Experiment (DIRBE; [Hauser et al. 1998](#)), which observed the sky in ten wavelength bands between 1.25 to 240 microns, with the primary aim to characterize the statistical properties of the Cosmic Infrared Background (CIB; [Partridge & Peebles 1967](#)). The CIB is thermal infrared radiation from both dust particles in distant galaxies and their redshifted starlight, and contains a large fraction of the total energy released in the Universe since the formation of galaxies. After an extended period of detailed analysis, clear CIB signatures were finally discovered in the DIRBE data, but confusion from both zodiacal light from the Solar system and thermal dust emission from the Milky Way made it difficult to fully reach DIRBE’s original goal ([Arendt et al. 1998](#); [Hauser et al. 1998](#); [Kelsall et al. 1998](#)). However, the fact that these emission processes are so bright also have ensured that the DIRBE data have had a far-reaching legacy value, and it remains one of the most important data sets for understanding zodiacal light emission to this date. The main goal of the work presented in this paper, and in its companion papers, is to resolve the most important and long-standing problems regarding the DIRBE data, and thereby finally release the full potential of these invaluable measurements.

Following DIRBE, almost a dozen other satellite experiments have targeted the same wavelengths with different angular resolution, sensitivity, and observation strategies, and today there exists a wealth of complementary and ancillary information that was not available between 1990 and 1994, when the official DIRBE analysis was completed. Two examples of such experiments are AKARI ([Murakami et al. 2007](#)), which covered six bands from 9 to 180 μm , and WISE ([Wright et al. 2010](#)), which covered four bands from 3.4 to 22 μm . Another important example of a recent and highly complementary experiment is the optical *Gaia* mission ([Gaia Collaboration et al. 2016](#)), which recently completed a deep survey of stars in the Milky Way ([Gaia Collaboration et al. 2018](#)).

Not only has great observational progress been made in terms of detailed measurements in the infrared regime during the last decades, but major breakthroughs have also been achieved both in terms of understanding the detailed structure of the Milky Way, and in how to analyse complex datasets optimally. One particularly striking example of this is provided by the cosmic microwave background (CMB) community, which through a long series of transformational experiments has revolutionized our understanding of the early universe; only a few examples include ACT ([Fowler et al. 2007](#)), BICEP/Keck ([BICEP2 Collaboration et al. 2014](#)), *COBE* ([Mather et al. 1994](#)), SPT ([Carlstrom et al. 2011](#)), and *WMAP* ([Bennett et al. 2013](#)). The current state-of-the-art in terms of full-sky CMB sensitivity is defined by ESA’s *Planck* satellite experiment ([Planck Collaboration I 2020](#)). However, precisely because of its exquisite signal-to-noise ratio, a long series of key data analysis challenges had to be overcome before its full cosmological potential could be released. Indeed, *Planck* was the first full-sky CMB experiment for which instrumental and astrophysical uncertainties dominated the total error budget, as opposed to white noise. As such, *Planck* faced many of the same types of problems that DIRBE had experienced two decades earlier, and massive amounts of algorithm development efforts were spent by hundreds of scientists on resolving these.

One of the main lessons learned from *Planck* was the importance of joint analysis of multiple complementary experiments, using information from one instrument to break the degenera-

cies in the others (e.g., [Planck Collaboration X 2016](#)). Building on that early ground-breaking work in *Planck*, a dedicated effort called COSMOGLOBE¹ was started, with a very simple basic idea: All radio, microwave and infrared experiments measure fundamentally the same sky. However, due to technical limitations, each experiment only measures a relatively small part of the electromagnetic spectrum, and with limited angular resolution and sensitivity. At the same time, the field as a whole is currently at a stage where astrophysical uncertainties play a dominating role in understanding the systematic properties of each experiment. It is therefore natural to expect that better results may be obtained by analyzing multiple complementary experiments together, as opposed to each separately, and in effect use information from one experiment to break the basic degeneracies in another. The long-term goal of the COSMOGLOBE effort is therefore to establish one single state-of-the-art model of the astrophysical sky that covers the entire electromagnetic spectrum, using all available experiments at the same time. This is a monumental task, and it will require the combined effort of the entire astrophysical community in order to be successful ([Gerakakis et al. 2023](#)).

A second important lesson learned from *Planck* was that, in order to properly mitigate all dominant systematic effects, it was no longer possible to consider each source of systematic uncertainty in isolation. Rather, it was necessary to perform a global integrated analysis in which all parameters are optimized simultaneously at the level of time-ordered data, whether they happen to be of instrumental or astrophysical origin. Two pioneering efforts in this direction were the SRo11 ([Delouis et al. 2019](#)) and NPIPE ([Planck Collaboration LVII 2020](#)) data analysis pipelines, both of which were developed within the official *Planck* consortium, and eventually formed the algorithmic basis for the *Planck* PR3 ([Planck Collaboration I 2020](#)) and PR4 ([Planck Collaboration LVII 2020](#)) data releases, respectively. In particular, both SRo11 and NPIPE integrated knowledge about the astrophysical sky directly in their instrument calibration and mapmaking steps, even though neither actually fitted the corresponding astrophysical parameters themselves during the low-level processing.

The first pipeline to perform true integrated global analysis of *Planck* data was implemented in a computer code called Commander3 ([Galloway et al. 2023](#)) by the BEYONDPLANCK collaboration ([BeyondPlanck Collaboration 2023](#)). This extended earlier work on Bayesian component separation that was performed within the *Planck* collaboration ([Planck Collaboration X 2016](#)), and was implemented in terms of an end-to-end Bayesian Monte Carlo Gibbs sampler in which an explicit parametric data model was fitted to raw uncalibrated time-ordered data (TOD). As a result of this integrated analysis, a number of long-standing problems regarding the *Planck* LFI data ([Planck Collaboration II 2020](#)) were resolved, in particular with respect to gain calibration, and the full LFI data set was now for the first time finally available for cosmological analysis ([Basyrov et al. 2023](#); [Colombo et al. 2023](#); [Paradiso et al. 2023](#)).

This line of work was subsequently generalized by [Watts et al. \(2023\)](#) to perform joint end-to-end Bayesian analysis of both the *WMAP* and *Planck* LFI data simultaneously. This turned out to be very effective, and the introduction of LFI measurements effectively resolved a number of long-standing calibration issues in the *WMAP* data that never could be resolved with *WMAP* data alone. The products from this analysis were released in March 2022 as “Cosmoglobe Data Release 1 (DR1)”, and de-

¹ <http://cosmoglobe.uio.no>

finest today the state-of-the-art in terms of both *Planck* LFI and *WMAP* sky maps.

The current paper is the first of a series of papers in which we perform a similar analysis for the *COBE*-DIRBE data, collectively referred to as COSMOGLOBE Data Release 2 (DR2). This work is a major step forward in the COSMOGLOBE program by expanding the modelled frequency range by three orders of magnitude, and it is a first step towards merging the microwave and infrared fields into one joint effort. The reasons for considering *COBE*-DIRBE in this first step, as opposed to AKARI, IRAS, or WISE, are two-fold. First and foremost, DIRBE has excellent systematic properties, both in terms of absolute calibration and zero-level determination, thermal stability, and in terms of a highly interconnected scanning strategy. At the same time, both its data volume and angular resolution are relatively modest, which makes the computational load and debugging cycle very manageable. Overall, DIRBE is an ideal dataset for generalizing the previous CMB-oriented model and computer code into the infrared regime.

At the same time, the fundamental challenges faced by DIRBE are very similar to those faced by any other infrared experiment. In particular, the single most challenging aspect is the zodiacal light (ZL) emission. This is thermal emission and scattered sunlight from interplanetary dust (IPD) grains. The main difficulty when dealing with zodiacal emission contamination in infrared data is that the observed emission is highly dependent on the position of the observer, and as such, it cannot be modeled like a static foreground, as for instance Galactic foregrounds are treated in the CMB community. Rather, the state-of-the-art method to remove zodiacal emission from timestreams today is to use a three-dimensional parametric interplanetary dust model which describes the distribution of interplanetary dust within the solar system, and perform line-of-sight integration for every single time step. The IPD model most widely used today is the so-called K98 model (Kelsall et al. 1998) produced by the DIRBE team, or variants thereof (e.g., Planck Collaboration XIV 2014). In a companion paper, San et al. (2024) present a major step forward in terms of ZL modelling for the DIRBE experiment, as a key component of the current COSMOGLOBE analysis. This progress is enabled by three main components. First, the usage of external data from *Planck*, WISE, and *Gaia* breaks key degeneracies between the ZL and the Galactic parameters. Second, fitting all parameters jointly with a modern Monte Carlo sampler allows the remaining degeneracies to be explored more efficiently than before. Third and finally, the current analysis characterizes and mitigates a source of excess radiation observed in the mid-infrared DIRBE channels that appears static in solar-centric coordinates. This radiation was noted already by Leinert et al. (1998), but no corrections have until now been implemented and applied to the DIRBE data. The net result is a greatly improved ZL model that should be of great utility to the entire infrared community.

These improvements also lead to better cosmological and astrophysical interpretation with the DIRBE data. For example, as part of the current data release Watts et al. (2024) derive improved constraints on the CIB monopole spectrum with DIRBE data, while Gjerløw et al. (2024a) present a new three-component model of thermal dust emission in the Milky Way that will be of great interest for the CMB community in the search for primordial gravitational waves. Similarly, Galloway et al. (2024) construct a new starlight model for DIRBE by combining WISE and *Gaia* data, that allow for robust modeling of the wavelength channels between 1.25 and 25 μm . Additionally, Gjerløw et al. (2024b) derive a full-sky map of ionized carbon

(C II) by combining spatial information in the DIRBE 140 μm channel with spectral measurements from the *COBE*-FIRAS instrument. While many issues still remain to be solved even after the current analysis, we argue that the products presented in the following redefines the standard for full infrared sky modelling, and the most of the methods described in the following are likely to be of direct use for the wide range of other infrared experiments, including AKARI, IRAS, and WISE. All products and computer codes are made publicly available² under an Open Source license.

The rest of the paper is organized as follows. In Sect. 2 we review the COSMOGLOBE data model and algorithms, and discuss the extensions needed for DIRBE analysis. In Sect. 3 we give an overview of the DIRBE instrument and data, as well as any pre-processing and data selection we apply to these, and in Sect. 4 we summarize the ancillary data sets used in the current processing. The actual results derived through this analysis are summarized in the next four sections. Section 5 discusses the basic Markov chains produced by the algorithm in terms of burn-in and convergence, while Sect. 6 focuses on instrumental noise estimation and overall goodness-of-fit. In Sect. 7 we provide the first systematic characterization of excess radiation for all DIRBE channels, and in Sect. 8 we present and characterize the new COSMOGLOBE DR2 ZSMA maps. Finally, we conclude and discuss avenues for future work in Sect. 9.

2. Global Bayesian modelling of the infrared sky

The use of Bayesian sampling methods have become widespread in the CMB community (e.g., Lewis & Bridle 2002; Dunkley et al. 2009; Handley et al. 2015; Planck Collaboration X 2016; Millea et al. 2019; Planck Collaboration VI 2020; Torrado & Lewis 2021; BeyondPlanck Collaboration 2023; Watts et al. 2023) during the last few decades for at least two important reasons. First, for any analysis task that may be phrased in terms of a classical parameter estimation problem with measured data \mathbf{d} and a model with some set of unknown parameters ω , the posterior distribution $P(\omega | \mathbf{d})$ is a complete summary of the information about ω contained in the current data, both in terms of best-fit point estimates and corresponding uncertainties. Second, both due to the innovation of a wide range of efficient Monte Carlo sampling methods and the exponential growth of computing power that took place until very recently, far more complex models can be mapped out today than was possible only one or two decades ago. As a particularly relevant case in point for the current paper is Commander (Eriksen et al. 2004; Seljebotn et al. 2019; Galloway et al. 2023), which is a Gibbs sampler designed to perform end-to-end analysis with time-ordered data. While the primary motivation for developing this machinery until today has been CMB-oriented applications, we show in the following that the same framework is also very well suited for analysis of observations in the infrared regime, and, indeed, that it may be used to construct one global model that includes both microwave and infrared wavelengths.

2.1. Data model and posterior distribution

The first step in any parametric Bayesian analysis is simply to write down a model for the data in question. The quality of the final results depends sensitively on the accuracy and completeness of this model, which must be monitored through detailed goodness-of-fit statistics, typically in the form of residual and

² <https://github.com/Cosmoglobe/>

χ^2 measures. In practice, an initial model is typically established based on a pre-existing knowledge about both the astrophysical sky and instrument in question, and the model is then gradually refined until the residuals are consistent with instrumental noise. The model described in this section is the product of such a process that has involved hundreds of trial runs, starting from a model very similar to that described by the official DIRBE and *Planck* teams, but then gradually generalized with new parameters. In particular, the current analysis follows closely in the footsteps of BEYONDPLANCK (BeyondPlanck Collaboration 2023) and COSMOGLOBE DR1 (Watts et al. 2023), which implemented the first version of this algorithm, and applied it to *Planck* LFI and *WMAP*, respectively. We refer the interested reader to those papers (and references therein) for complete algorithmic details.

As described in Sect. 3, we will in the current analysis focus on the so-called DIRBE Calibrated Individual Observations (CIOs). Ideally, the optimal approach would in principle be to start from raw uncalibrated TOD, but those are not publicly available. In addition, the CIO are easier to work with, since they have been cleaned from low-level instrumental effects. On the other hand, we note that this immediately implies that there are important degrees of freedom, in particular with respect to gain and zero-level determination, that rely directly on the official analysis, and that may need to be revisited at a later stage. On the other hand, the main residuals that emerge at the end of the current analysis still appear to be dominated by astrophysical confusion rather than gain errors, and moving on to uncalibrated TOD is therefore not yet a top priority. We will in the following refer to the DIRBE CIOs simply as “TOD”.

2.1.1. TOD model

We adopt the following high-level parametric data model for the DIRBE TOD,

$$\mathbf{d} = \mathbf{GPB} \sum_{c=1}^{n_{\text{comp}}} \mathbf{M}_c \mathbf{a}_c + \mathbf{s}_{\text{zodi}} + \mathbf{s}_{\text{static}} + \mathbf{n}_{\text{corr}} + \mathbf{n}_w \quad (1)$$

$$\equiv \mathbf{s}_{\text{tot}} + \mathbf{n}_w, \quad (2)$$

where \mathbf{d} denotes a stacked vector of all DIRBE TOD for all frequency bands; \mathbf{G} is an $n_{\text{tod}} \times n_{\text{tod}}$ diagonal matrix with an overall constant gain calibration factor per frequency channel; \mathbf{P} denotes a satellite pointing matrix, which we define in Galactic coordinates; \mathbf{B} denotes an instrumental beam (or point spread function) convolution operator; the sum runs over n_{comp} astrophysical components, each with a free amplitude \mathbf{a}_c at some reference frequency and a mixing matrix \mathbf{M}_c which defines the effective scaling from the reference frequency to an observed frequency for each component, taking into account the bandpass of each detector; \mathbf{s}_{zodi} is a model of zodiacal light emission from components that appear time-variable as seen from Earth (e.g., the zodiacal cloud and asteroidal bands); $\mathbf{s}_{\text{static}}$ is an excess signal that appears stationary with respect to the Earth-Sun system, discussed further in Sect. 7; \mathbf{n}_{corr} is correlated instrumental noise (which for now is only fitted for the lowest DIRBE frequency channel); and \mathbf{n}_w denotes white instrumental noise. We also define \mathbf{s}_{tot} to be the sum of all terms in the data model except for the white noise.

As we work with calibrated TOD, we set $\mathbf{G} = \mathbf{I}$ for now, but note that this effective prior should be relaxed in future work, for instance by using *COBE-FIRAS* data as a calibration source in the overlap frequency range between *FIRAS* and *DIRBE*. Similarly, both the pointing \mathbf{P} and the beam operator \mathbf{B} are provided

by the DIRBE team, and we do not account for any uncertainties in these. However, we do note that the DIRBE beams have an intrinsically square shape, while our current beam convolution implementation only supports azimuthally symmetric beams. This will necessarily lead to a residual that should ideally be accounted for through full beam integration, for instance using a conviqt-style algorithm (Prézeau & Reinecke 2010; Keihänen & Reinecke 2012); this is left for future work. Similar remarks apply to bandpass definitions as well; for now, we neglect the uncertainty in the bandpass profiles provided by the DIRBE team. For further details regarding the pointing, beam and bandpasses, see Sect. 3.

The sky model is described in detail by Galloway et al. (2024) and Gjerløw et al. (2024a), and reviewed briefly in Sect. 2.1.2. We define the set of all linear sky component amplitude parameters as \mathbf{a}_{sky} and the set of all spectral parameters as β_{sky} in the following.

Our model for zodiacal light emission, \mathbf{s}_{zodi} , is described by San et al. (2024), and the overall framework follows closely that introduced by Kelsall et al. (1998) (denoted “K98” in the following) for the original DIRBE analysis. Specifically, we fit a limited number of shape parameters per interplanetary dust component, such as a smooth cloud and asteroidal bands, in addition to linear emissivity and albedo parameters for each frequency channel. In total, there are 64 free parameters in this model, and these are collectively denoted ζ_z .

The term denoted $\mathbf{s}_{\text{static}}$ has not been included in previous DIRBE analyses, but is rather an important novel feature presented in the current paper. We will return to its physical interpretation in Sect. 7, but note for now that it models excess radiation in the DIRBE channels between 4.9 and 60 μm not accounted for in the K98 model. In practice, this is implemented in terms of a pixelized map, $\mathbf{a}_{\text{static}}$, in solar-centric coordinates, such that $\mathbf{s}_{\text{static},\nu} = \mathbf{P}_{\text{sol},\nu} \mathbf{a}_{\text{static},\nu}$, where $\mathbf{P}_{\text{sol},\nu}$ is the pointing matrix rotated into a coordinate system where the Sun is always at coordinates $(l, b) = (0^\circ, 0^\circ)$, and the Ecliptic plane is aligned with the equator. The amplitude map, $\mathbf{a}_{\text{static},\nu}$, is fitted independently for each frequency channel.

Next, we assume that the instrumental noise is piecewise stationary, and we model it with an uncorrelated zero-mean Gaussian distribution with a free standard deviation per sample, σ_n for all channels except 240 μm . The stationarity period is assumed to be 24 hours, and the data are correspondingly processed in segments of this length. For the 240 μm channel we additionally include a correlated noise term. We assume that the time-domain noise power spectrum of this component may be described by a standard $1/f$ profile of the form $P(f) = \sigma_n^2 (1 + (f/f_{\text{knee}})^\alpha)$, where the slope α and knee frequency f_{knee} are fitted independently in each data segment. Ideally, we would like to include this component in all frequencies. However, we find that the current sky model is not yet a sufficiently good fit at any of the other channels. In total, we denote the sum of all noise parameters by ξ_n .

2.1.2. Sky model

The sky signal defined implicitly by the sum in Eq. (1) is defined by Galloway et al. (2024) and Gjerløw et al. (2024a), and reads

as follows in units of brightness temperature and frequency,³

$$\begin{aligned}
\sum_{c=1}^{n_{\text{comp}}} M_c \mathbf{a}_c &= M_{\text{mbb}}(\beta_c, T_c, q_i; \nu_{0,c}, \{\Delta\nu_i\}) \mathbf{a}_{\text{cold}} && \text{(Cold dust)} \\
&+ M_{\text{mbb}}(\beta_h, T_h, q_i; \nu_{0,h}, \{\Delta\nu_i\}) \mathbf{a}_{\text{hot}} && \text{(Hot dust)} \\
&+ M_{\text{mbb}}(\beta_n, T_n, q_i; \nu_{0,n}, \{\Delta\nu_i\}) \mathbf{t}_{\text{near}} a_\nu && \text{(Nearby dust)} \\
&+ \left(\frac{\nu_{0,\text{ff}}}{\nu}\right)^2 \frac{g_{\text{ff}}(\nu; T_e)}{g_{\text{ff}}(\nu_{0,\text{ff}}; T_e)} \mathbf{t}_{\text{ff}} && \text{(Free-free)} \\
&+ \delta(\nu - \nu_{0,\text{CO}}^i) \mathbf{t}_{\text{CO}} h_{\nu,i}^{\text{CO}} && \text{(CO)} \\
&+ \delta(\nu - \nu_{0,\text{C II}}) \mathbf{a}_{\text{C II}} h_\nu^{\text{C II}} && \text{(C II)} \\
&+ U_{\text{mJy}} \sum_{j=1}^{n_s} f_{\text{Gaia},j} a_{s,j} && \text{(Bright stars)} \\
&+ U_{\text{mJy}} \mathbf{t}_{\text{Gaia,fs}} a_{\text{fs},\nu} && \text{(Faint stars)} \\
&+ U_{\text{mJy}} \sum_{j=1}^{n_e} M_{\text{mbb}}(\beta_{e,j}, T_{e,j}) a_{e,j} && \text{(FIR sources)} \\
&+ m_\nu && \text{(Monopole)}.
\end{aligned}$$

In this expression, we have defined a function of the form

$$M_{\text{mbb}}(\beta, T, q_i; \nu_0, \{\Delta\nu_i\}) = \begin{cases} q_i & \nu \in \Delta\nu_i \\ \left(\frac{\nu}{\nu_0}\right)^{\beta+1} \frac{e^{h\nu_0/k_B T} - 1}{e^{h\nu/k_B T} - 1} & \nu \notin \Delta\nu_i, \end{cases} \quad (3)$$

which represents a generalized modified blackbody function. However, in addition to the usual emissivity index and temperature, β and T , this function takes a set of constant values, q_i , and corresponding frequency ranges $\Delta\nu_i$. If the requested frequency happens to lie in any one of $\Delta\nu_i$, then q_i is returned; otherwise the default is to return the standard modified blackbody spectrum. Another point to note in the above equation is that if a given amplitude is denoted by \mathbf{a} , then it is fitted freely to the current data; if it is denoted by \mathbf{t} , it is fixed to an external template.

As indicated by the above sky model, we fit a novel three-component generalized modified blackbody model to account for thermal dust emission across the combined DIRBE and *Planck* HFI frequency range; for full details, see [Gjerløw et al. \(2024a\)](#). The three components correspond to cold dust, hot dust, and nearby dust emission, respectively. All three are modeled with spatially constant spectral parameters, and only the cold and hot component amplitudes are fitted pixel-by-pixel; the amplitude of the nearby component is fixed to the *Gaia*-based dust extinction template covering distances up to 1.25 kpc produced by [Edenhofer et al. \(2024\)](#). As such, this dust model has in fact only two degrees of freedom per pixel, in addition to fewer than 30 spatially constant SED parameters. This is an extremely economical model of thermal dust emission, considering the fact that it describes the entire combined frequency range covered by both *Planck* HFI and DIRBE, from 100 GHz to 1 μm .

To account for free-free emission, we adopt the model presented by [Planck Collaboration IX \(2016\)](#), both in terms of spatial distribution and spectrum. The SED of this component is defined by the Gaunt factor, $g_{\text{ff}}(\nu; T_e)$ ([Dickinson et al. 2003](#); [Draine 2011](#)), which corresponds to a shift in the spectral index

³ Due to its CMB-oriented origin, *Commander* uses brightness temperature and frequency units for internal calculations, rather than flux density and wavelength units which would be more natural for DIRBE. This has, however, no actual effect on the final results, but only requires appropriate unit conversions to be applied during input and output operations.

of about -0.14 in the CMB frequency range; however, at the very high DIRBE frequencies of up to 300 THz, it takes on significantly more extreme values, and this should at least in principle provide greater sensitivity to the electron temperature, T_e . For now, however, we adopt the T_e distribution presented by [Planck Collaboration IX \(2016\)](#) as given, and will rather attempt to actually fit T_e in future work.

The next component corresponds CO line emission, produced by transitions between two quantized angular momentum eigenstates in the CO molecule. The resulting emission forms effectively a ladder in frequency space in multiples of 115.27 GHz, and *COBE-FIRAS* identified emission all the way up to 922 GHz, albeit with low sensitivity and angular resolution. In contrast, *Planck* produced high-resolution maps with high sensitivity of the $J=1\leftarrow 0$, $2\leftarrow 1$, and $3\leftarrow 2$ transitions, which contributed to the HFI 100, 217, and 353 GHz frequency maps, but was unable to identify CO emission at higher frequencies due to strong thermal dust emission. In the current work, we adopt the [Dame et al. \(2001\)](#) CO $J=1\leftarrow 0$ map as a fixed tracer for all variations of CO emission, and we also adopt the line ratios, $h_{\nu,i}$, presented by [Planck Collaboration X \(2016\)](#) for the 100, 217, and 353 GHz *Planck* channels. As far as the current analysis is concerned, the CO component is thus a fixed correction applied to the relevant *Planck* bands.

Similarly, the fourth component corresponds to C II line emission, which has a rest frequency of 1900 GHz. As such, it only affects the DIRBE 140 μm map in our dataset, in addition to selected FIRAS bands. In this case, we fit for a free amplitude per pixel with DIRBE 140 μm , using the general sky model determined by near-by channels to remove thermal dust emission, and then exploit the near-by FIRAS channels to monitor the overall reconstruction quality. The result is a novel full-sky C II map with an angular resolution of about 1° FWHM.

The fifth and sixth components correspond to starlight emission, which is relevant in the frequency range between 1 and 25 μm ; for full details regarding this model, see [Galloway et al. \(2024\)](#). For these, we first extract a baseline star catalog by thresholding the AllWISE 3.5 μm catalog at magnitude 8, resulting in a set of about 783 000 sources.⁴ For each of these, we search the *Gaia* DR2 catalog, and if this returns a positive star identification within a radius of 20 arcsec, we record the object, and store the best-fit temperature T_s , surface gravity g , and metallicity [M/H] as determined by *Gaia*. These are then used to estimate the best-fit SED using the PHOENIX spectrum grid ([Husser et al. 2013](#)), which is convolved with the bandpass and beam profile of each DIRBE channel. The resulting bandpass- and beam-convolved SED is denoted $f_{\text{Gaia},j}$, which is unique for each star. We then fit one overall amplitude for each star to the four highest DIRBE frequency bands between 1.25 and 4.9 μm ; we also account for star emission in the 12 and 25 μm bands, but these bands are not used for the actual fit. A total of 717 000 stars are included in the fit of individual stars; these are denoted as “bright stars” in the sky model.

The remaining 66 000 bright WISE sources that do not have a *Gaia* counterpart are fitted with a standard modified blackbody spectrum across the same frequency range, as described by the line marked by “FIR sources” in the sky model. Algorithmically speaking, this component is identical to the bright star component, except for the parametric form of the SED.

⁴ We have tried different thresholds, and found that magnitude 8 provides a good compromise; magnitude 6 results in obviously missing sources, while magnitude 10 leads to too many unconstrained sources.

The AllWISE catalog itself contains a total of about 747 million sources, making it impossible to fit all of these with DIRBE without introducing massive degeneracies. We therefore instead co-add the rest of the AllWISE sources into a diffuse background map of faint sources under the assumption that their mean SED is equal to the average of the bright sources that actually are fitted as part of the algorithm. Together, these three source components comprise an unprecedented deep model for compact objects in DIRBE that has only become possible due to WISE and *Gaia*.

The tenth and final component is simply a monopole per frequency. For DIRBE and FIRAS, this should ideally describe the CIB spectrum, but it is also sensitive to zodiacal light and Galactic residuals. DIRBE was designed to have negligible straylight contamination, while internal thermal sources in FIRAS were explicitly measured by onboard thermistors and subtracted before mapmaking. For *Planck*, the monopoles account for the arbitrary zero-levels present in the *Planck* PR4 maps.

Finally, it is worth noting that there is no CMB component present in the current sky model, even though it applies to the *Planck* HFI as well as DIRBE. Since the main focus in the current work is DIRBE, we have chosen to pre-subtract any CMB component (including the solar CMB dipole and relativistic quadrupole corrections) from each frequency map. For this, we use the PR3 Commander CMB maps (Planck Collaboration IV 2018). Similarly, we neglect the impact of synchrotron emission, anomalous microwave emission, the Sunyaev-Zeldovich effect, and other smaller contributions; these will instead be included in a future analysis that also has HFI as a main science target.

2.1.3. Posterior distribution

In principle, all quantities on the right-hand side of Eq. (1) are associated with free parameters and uncertainties that should be estimated from the data, whether they are of astrophysical or instrumental origin. We define the full set of free parameters as $\omega = \{\mathbf{G}, \xi_n, \beta_{\text{sky}}, \mathbf{a}_{\text{sky}}, \zeta_z, \mathbf{a}_{\text{static}}\}$, and our goal is now to derive an explicit expression for the global posterior distribution, $P(\omega | \mathbf{d})$. This is most easily done through Bayes' theorem,

$$P(\omega | \mathbf{d}) = \frac{P(\mathbf{d} | \omega)P(\omega)}{P(\mathbf{d})} \propto \mathcal{L}(\omega)P(\omega). \quad (4)$$

In this expression, $\mathcal{L}(\omega) \equiv P(\mathbf{d} | \omega)$ is called the likelihood, $P(\omega)$ is called the prior; $P(\mathbf{d})$, called the evidence, is a normalization constant that does not depend on ω , which we neglect in this work.

Under the common assumption that the white noise component is Gaussian distributed with zero mean and some covariance matrix, \mathbf{N}_w , we can write the log-likelihood in the usual explicit form,

$$-2 \ln \mathcal{L}(\omega) = (\mathbf{d} - \mathbf{s}^{\text{tot}}(\omega))^T \mathbf{N}_w^{-1} (\mathbf{d} - \mathbf{s}^{\text{tot}}(\omega)) + \ln |\mathbf{N}_w|, \quad (5)$$

once again up to an irrelevant normalization constant, and we have for notational compactness suppressed the fact that also \mathbf{N}_w has free parameters.

Regarding $P(\omega)$, we will in this analysis operate primarily with three types of priors. First, for zodiacal light parameters we adopt uniform priors between pre-defined limits, to avoid the algorithms to diverge into pathological solutions. Second, for astrophysical spectral parameters, such as temperature and spectral indices, we adopt products of uniform priors with broad limits and Gaussian priors with spectral parameters informed by

Planck where applicable. Finally, for a few select astrophysical components, for instance free-free and carbon monoxide line emission, we adopt existing spatial templates as delta function priors on the spatial morphology, and only fit overall free amplitudes in the current analysis. For full details regarding the use of priors for a given component, we refer the interested reader to Galloway et al. (2024) and Gjerl w et al. (2024a).

2.2. Gibbs sampling with Commander3

As described in Sect. 2.1, the current data model contains millions of strongly correlated parameters, ranging from affecting individual time samples (such as the correlated noise, \mathbf{n}_{corr}) to describing the astrophysical signal in the form of a pixelized map (such as the cold dust amplitude \mathbf{a}_c) or a catalog (such as the bright star amplitude \mathbf{a}_s), to simultaneously affecting essentially every single data point, such as the zodiacal light shape parameters. Mapping out this distribution is therefore highly non-trivial.

So far, the only algorithm that has been demonstrated in practice to work well on such complex end-to-end analysis problems (BeyondPlanck Collaboration 2023; Watts et al. 2023) is Gibbs sampling (e.g., Geman & Geman 1984), which is a special case of the Metropolis-Hastings sampling algorithm. The defining feature of this algorithm is that it loops over all free parameters (which may be divided into groups), and draws a sample from each conditional distribution. Returning to the defining data model in Eq. (1), and recalling that the set of free parameters is $\omega = \{\xi_n, \beta_{\text{sky}}, \mathbf{a}_{\text{sky}}, \zeta_z, \mathbf{a}_{\text{static}}\}$, we can immediately write down a corresponding Gibbs sampling chain of the following form:

$$\xi_n \leftarrow P(\xi_n | \mathbf{d}, \beta_{\text{sky}}, \mathbf{a}_{\text{sky}}, \zeta_z, \mathbf{a}_{\text{static}}) \quad (6)$$

$$\beta_{\text{sky}} \leftarrow P(\beta_{\text{sky}} | \mathbf{d}, \xi_n, \mathbf{a}_{\text{sky}}, \zeta_z, \mathbf{a}_{\text{static}}) \quad (7)$$

$$\mathbf{a}_{\text{sky}} \leftarrow P(\mathbf{a}_{\text{sky}} | \mathbf{d}, \xi_n, \beta_{\text{sky}}, \zeta_z, \mathbf{a}_{\text{static}}) \quad (8)$$

$$\zeta_z \leftarrow P(\zeta_z | \mathbf{d}, \xi_n, \beta_{\text{sky}}, \mathbf{a}_{\text{sky}}, \mathbf{a}_{\text{static}}) \quad (9)$$

$$\mathbf{a}_{\text{static}} \leftarrow P(\mathbf{a}_{\text{static}} | \mathbf{d}, \xi_n, \beta_{\text{sky}}, \mathbf{a}_{\text{sky}}, \zeta_z). \quad (10)$$

Here, the symbol \leftarrow indicates drawing a sample from the conditional distribution on the right-hand side. However, we note that our codes are also designed to perform maximum-posterior (or likelihood) analysis, in which case we maximize the probability distribution instead of drawing a sample from it.

The current state-of-the-art implementation in terms of CMB Gibbs sampling is Commander (Eriksen et al. 2004), which was used extensively for the *Planck* analysis. However, during the *Planck* analysis this code only supported high-level component separation operations, and the low-level time-domain support was added after the official end of *Planck*. The first incarnation of this end-to-end framework is called Commander3 (Galloway et al. 2023), which was applied to the *Planck* LFI data by the BEYONDPLANCK collaboration (BeyondPlanck Collaboration 2023). Shortly after, a slightly extended version was applied to the combination of *Planck* LFI and WMAP by Watts et al. (2023), and the results from this analysis formed the basis for COSMOGLOBE DR1.

The existing Commander3 implementation used for BEYONDPLANCK and COSMOGLOBE DR1 already provides sampling steps for most of the above conditional distributions, and these can be reused with minimal modifications. In particular, Gjerl w et al. (2023) describe how to sample instrumental gain; Ihle et al. (2023) describe how to estimate instrumental noise parameters, and Keih nen et al. (2023) discuss how to make optimal maps with full noise propagation efficiently with Gibbs sampling; finally Andersen et al. (2023) describe how to sample from intensity foregrounds posteriors.

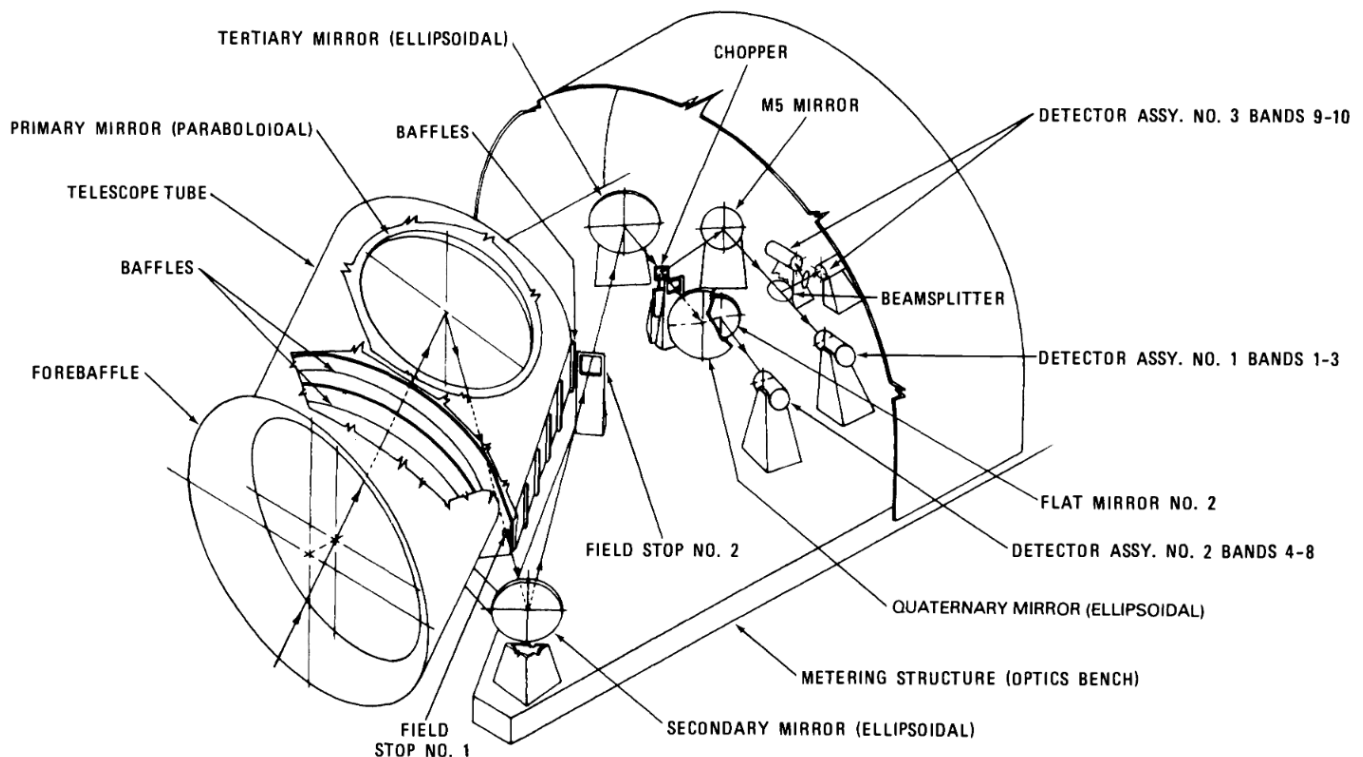


Fig. 1. DIRBE optics module. The optical design includes two field stops, one of which is square, to reduce straylight contamination. Reproduced from [Magner \(1987\)](#).

Table 1. List of celestial body flags.

Object	Radius (°)
Moon	10
Mercury	1
Venus	2
Mars	2
Jupiter	2
Saturn	1
Uranus	1
Neptune	1

While by far most of the code infrastructure required to process the DIRBE TOD already exists, several of these steps and models discussed above require slight modifications in order to work efficiently in a production environment. In particular, efficient diffuse foreground sampling for DIRBE is described by [Gjerløw et al. \(2024a\)](#) and the novel starlight model and sampler are described by [Galloway et al. \(2024\)](#).

The ZL sampling step described by Eq. (9), however, did not have support in the existing `Commander` implementation until the current work, and had to be developed from scratch. An early step towards this goal was described by [San et al. \(2022\)](#), who reimplemented the default DIRBE zodiacal light model (K98; [Kelsall et al. 1998](#)) in Python. This served as the basis for the code developed here, which now is a set of native `Commander` modules written in Fortran. The full details of the new zodiacal light estimation framework, including a significantly improved best-fit model with respect to K98, is presented by [San et al. \(2024\)](#).

Similarly, the sampling step for the static component amplitude, $\mathbf{a}_{\text{static}}$, also had to be developed from scratch for the current

work. However, in contrast to the ZL sampler, which required a non-trivial amount of coding effort, the algorithm for $\mathbf{a}_{\text{static}}$ is very straight-forward. Based on the data model in Eq. (1), we first compute a residual that removes all components except $\mathbf{s}_{\text{static}}$,

$$\mathbf{r}_{\text{static}} = \mathbf{d} - \left[\text{GPB} \sum_{c=1}^{n_{\text{comp}}} \mathbf{M}_c \mathbf{a}_c + \mathbf{s}_{\text{zodi}} + \mathbf{n}_{\text{corr}} \right], \quad (11)$$

and we then bin this time-ordered residual in solar-centric coordinates according to the usual map-making equation for Gaussian noise (e.g., [Tegmark 1997](#)). Explicitly, the appropriate Gibbs sample is given by (see, e.g., Appendix A in [Beyond-Planck Collaboration 2023](#))

$$(\mathbf{P}_{\text{sol}}^t \mathbf{N}_{\text{wn}}^{-1} \mathbf{P}_{\text{sol}}) \mathbf{a}_{\text{static}} = \mathbf{P}_{\text{sol}}^t \mathbf{N}_{\text{wn}}^{-1} \mathbf{r}_{\text{static}} + \mathbf{P}_{\text{sol}}^t \mathbf{N}_{\text{wn}}^{-\frac{1}{2}} \boldsymbol{\omega}, \quad (12)$$

where $\boldsymbol{\omega} \sim N(0, 1)$ is a vector of standard Gaussian variates. Since the white noise component by definition is uncorrelated, this equation may be solved pixel-by-pixel.

3. Diffuse Infrared Background Experiment

3.1. The DIRBE instrument

The Diffuse InfraRed Background Experiment (DIRBE) was one of three experiments on the Cosmic Background Explorer (*COBE*) satellite ([Boggess et al. 1992](#)). DIRBE was designed to characterize the infrared sky from $1 \mu\text{m}$ to $240 \mu\text{m}$, with the sensitivity required to characterize thermal dust emission, zodiacal emission, and to detect the CIB ([Silverberg et al. 1993](#)). The DIRBE experiment was limited by its cryogenic requirement, using 600 L of superfluid ^4He , cooling the instrument to 1.6 K.

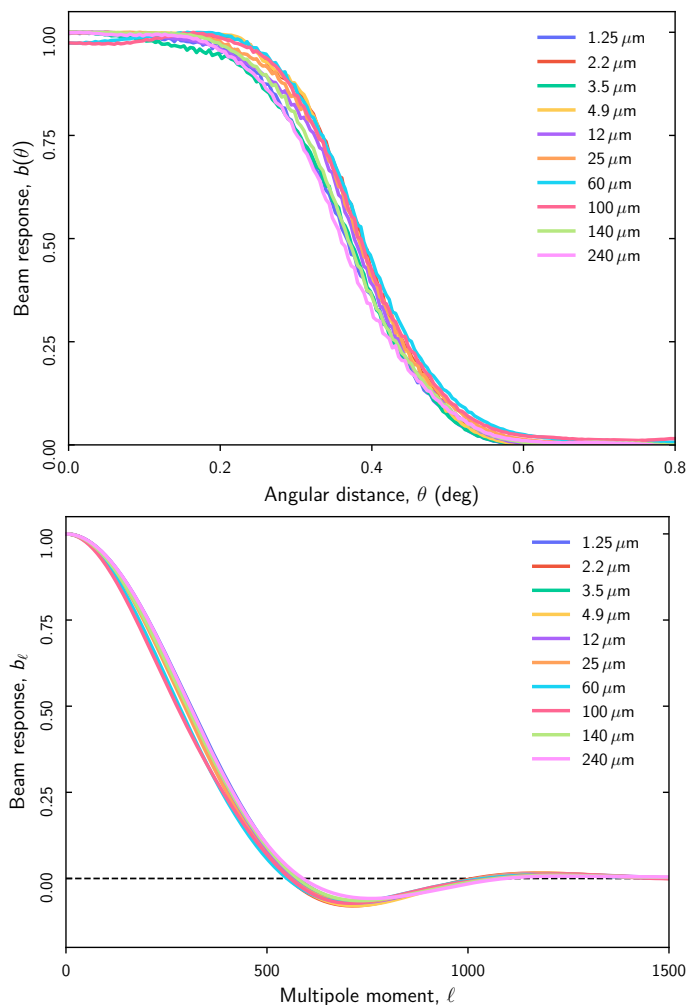


Fig. 2. Symmetrized beam response functions for each DIRBE channel, both in real space (*top*) and in harmonic space (*bottom*).

3.2. Pointing, beam and bandpass response

The *COBE* satellite followed a Sun-synchronous orbit at 900 km, orbiting the Earth at a 99° inclination every 103 minutes. The spacecraft rotated around its axis at a rate of 0.8 rpm, with the DIRBE optics pointed 30° from the spin axis. Due to the orientation changes of the satellite throughout this orbit, DIRBE was able to observe approximately half the sky during the day at solar elongation angles of 64° – 124° . The pointing was determined by interpolating on-board gyroscopic data with the positions of known stars in the short-wavelength bands.

The DIRBE optical design included several design solutions for calibration and stray light reduction. Straylight reduction was prioritized in the design, largely because of the difficulty in distinguishing this systematic effect from a true diffuse background. In particular, there are several straylight stops to reduce sidelobe contamination, mainly in the form of a square beam, as can be seen in Fig. 1. In addition to the straylight reduction, DIRBE alternates observations between the sky and an internal calibration source that chops between the two light sources at a rate of 32 Hz. All bands observe the same $0^\circ.7 \times 0^\circ.7$ field simultaneously, with small adjustments of the beam centroids depending on the location of the detectors. The light is divided using beam splitters to split the light into various detector assemblies. Detectors 1–3 were polarization-sensitive, with light parallel and perpendicular to the scan direction being detected. Because of the DIRBE

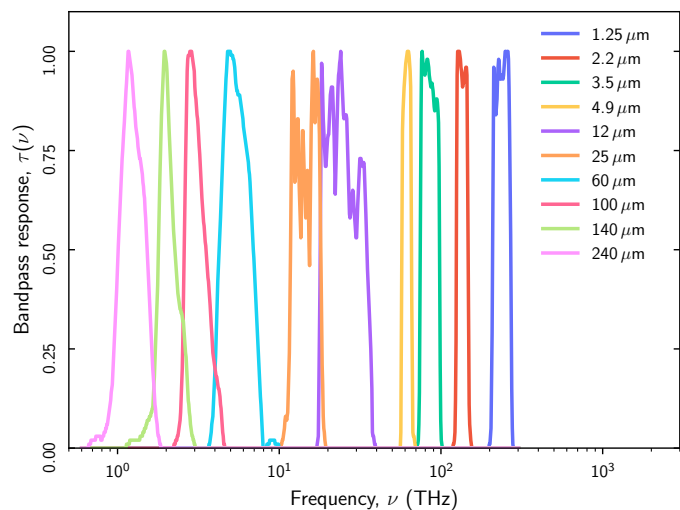


Fig. 3. Bandpass response functions for each DIRBE channel, plotted as a function of frequency.

scan strategy, the resulting maps show poor polarization angle coverage across the sky.

The symmetrized beam, shown in the top panel of Fig. 2, resembles a tophat with a slow falloff. The harmonic-space representation of the beam is therefore reminiscent of a sinc function, with oscillations about zero above $\ell \gtrsim 500$. For a band-limited signal to be characterized fully in map space, the $42'$ DIRBE beams must be represented with a $21'$ or smaller pixelization. However, in order to be fully characterized in harmonic space, a requirement for the Commander3 multi-resolution component separation, the pixelization scheme must have support up to $\ell \lesssim 1500$. The original DIRBE maps have pixel size of $21'$, insufficient for harmonic space analysis. Neither the original maps in Quadcube⁵ pixelization (resolution 9, pixel size $21'$) nor the CADE⁶ reprojection into HEALPix ($N_{\text{side}} = 256$, pixel size $13.7'$) have the required support over the full multipole range.

The DIRBE central bandpasses, given in terms of central frequency and central wavelength, are given in Table 3, and the full bandpass responses as reported in Hauser et al. (1998) are shown in Fig. 3. The different detector technology for each band accounts for the different performances and systematics found in each of the bands. Silverberg et al. (1993) in particular highlight the Ge:Ga photoconductors' (bands 7 and 8) response to ionizing radiation in the South Atlantic Anomaly (SAA) being worse than other detectors, requiring long time for the detectors to return to normal. Similarly, the use of a composite Si bolometer for bands 9 and 10 partially explain the over an order of magnitude increase in noise when compared to adjacent bands.

3.3. Data selection and masking

In order to produce maps with full multipole support, we analyze the CIOs directly and convert the pointing into $7' N_{\text{side}} = 512$ pixels from the native resolution 15 Quadcube pixels with $20''$ in the delivered CIOs.⁷ The conversion from CIO pixel indices to Galactic longitude and latitude is detailed in Hauser et al.

⁵ Quadrilateralized Spherical Cube https://lambda.gsfc.nasa.gov/product/cobe/skymap_info_new.html

⁶ Centre d'Analyse de Données Etendues, <http://cade.irap.omp.eu/dokuwiki/doku.php?id=dirbe>

⁷ https://lambda.gsfc.nasa.gov/product/cobe/dirbe_cio_data_get.html

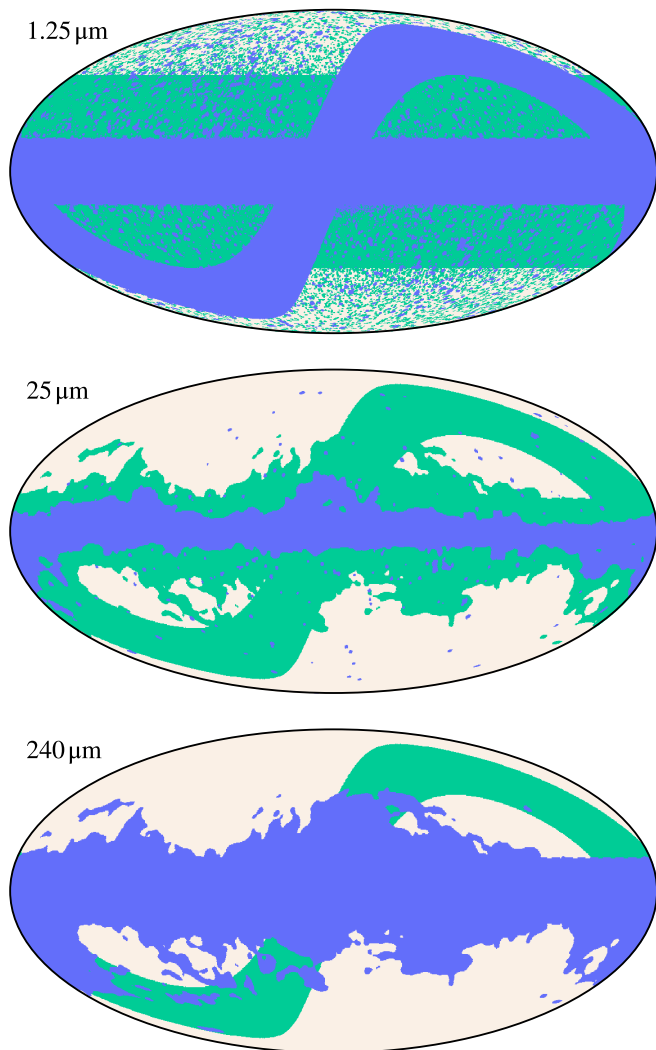


Fig. 4. Processing masks used in the analysis. Green regions correspond to the general TOD processing masks, and the blue regions correspond to the zodiacal emission masks. In the $240\ \mu\text{m}$ band, the zodiacal emission mask includes the entirety of the general TOD processing mask.

(1998), and is reimplemented in the Python preprocessing script `quadcube`.⁸

The delivered CIOs are organized into 285 single-day files, with the datapoints ordered by `Quadcube` pixel index. The primary processing step was converting the pointing into $N_{\text{side}} = 512$ pixels using `quadcube`. The data are sampled at 8 Hz and labeled by time index in seconds since January 1, 1981 00:00 UTC. Because the data are pre-calibrated and bad data are already removed, there are some gaps in the data, which we fill manually with an appropriate flag. Additional flags, such as excess noise, orbit and attitude errors, and presence of the SAA, are additionally extracted. In total, the data are placed in one `hdf5` file per band, following the format enumerated in Galloway et al. (2023). The planet flags are not present in the CIOs, and are regenerated beforehand. Using the radii as defined in Table 1, we mark data points within the pointing of each pixel. Note that this is not strictly optimal due to the non-circular beam shape, and can be optimized in future analyses.

⁸ <https://github.com/MetinSa/quadcube>

4. Ancillary data sets

As demonstrated by the success of the BEYONDPLANCK and COSMOGLOBE projects, the use of complementary datasets with different angular resolution, frequency coverage, and observation strategies, can greatly improve the quality of low-level data processing. In this work, we use *Planck* High Frequency Instrument, WISE, *Gaia*, and *COBE-FIRAS* to better constrain our sky model and characterize the DIRBE data.

4.1. *Planck* HFI

The *Planck* High Frequency Instrument (HFI; Planck Collaboration III 2020) observed the sky in six channels from 100 GHz to 857 GHz from May 2009–2013, with angular resolution of $10' - 4'$. While the primary purpose of the *Planck* mission was to characterize fluctuations in the CMB, a large part of its scientific legacy comes from its observations of the far-infrared sky, with robust characterization of the Milky Way (Planck Collaboration Int. XVII 2014; Planck Collaboration X 2016; Planck Collaboration III 2020) and of CIB fluctuations (Planck Collaboration X 2016; Planck Collaboration Int. XVII 2014; Lenz et al. 2019; McCarthy 2024).

In addition to its complementary observation strategy, *Planck*'s frequency coverage has a relatively lower expected amount of zodiacal emission, with a total expected amplitude of $\lesssim 1\%$ before any subtraction (Maris et al. 2006; Planck Collaboration XIV 2014), as compared to almost 100% of the signal in some DIRBE bands. All delivered *Planck* maps have had an estimate of the zodiacal emission modeled using the 3D model derived by K98 with varying emissivities per component. While this technically is redundant information that could contaminate this joint analysis, the already low amplitude of zodiacal emission in the HFI maps limits the potential impact of using a technically incorrect zodiacal emission model. A full analysis fitting for zodiacal emission parameters using both HFI and DIRBE will be left for future work.

At the same time, CIB fluctuations with a similar SED to the Milky Way have been detected with high significance in the HFI data, and are directly visible in 353–857 GHz maps at high Galactic latitudes. Incorrectly modeled, this could bias the Galactic thermal dust model and lead to an incorrect model of the sky in the DIRBE range. In order to avoid this, we remove the GNILC (Planck Collaboration Int. XLVIII 2016) estimate of the CIB from the HFI maps before including them in our analysis.

Since this work is primarily concerned with the DIRBE dataset, the modeling of CMB temperature fluctuations gives an unnecessary degree of freedom to be marginalized over. Therefore, we subtract the `Commander3` PR3 CMB temperature estimate from the *Planck* HFI maps, effectively conditioning the entire Gibbs chain on this CMB estimate. We use single *Planck* detector maps to avoid the complication of subtle bandpass mismatches between nearby detectors. In total, we use the 100-1, 217-1, and 353-1 temperature maps and the total 545 GHz and 857 GHz maps, all from the PR4 release (Planck Collaboration LVII 2020).

4.2. *Gaia* and WISE

In the near-infrared, most of the sky observed by DIRBE consists of stars and point sources. We therefore use catalogs derived from external datasets as fixed locations of each source, while fitting for the amplitudes in the Gibbs chain. As of this publication,

the most complete catalog of stars in the Milky Way comes from the *Gaia* mission (Gaia Collaboration et al. 2016, 2018). In particular, physics models of 100 million stars are provided in *Gaia* DR2. Despite *Gaia* operating between 330–1050 nm, these models can be used as informative priors for the amplitude of stars at the DIRBE near-infrared bands. With a limiting magnitude of $G \sim 20$ across the entire sky, this star catalog gives a complete survey of all stars that are detectable within the DIRBE bands.

Conversely, the WISE satellite (Wright et al. 2010) has mapped the sky at 3.4, 4.6, 12, and 22 μm , with resolutions of $6''.11$, $6''.4$, $6''.5$, and $12''.0$. This gives a direct estimate of point source brightness and location, and allows for direct cross-matching with the *Gaia* DR2 catalog. In order to leverage the *Gaia* data properly, we extract the SED for point sources in both *Gaia* and WISE with < 8 mag at 3.4 μm . These SEDs are then scaled directly per star in the Gibbs chain to correct for absolute calibration differences between the *Gaia*+WISE catalog and DIRBE. There are a total of 717 454 stars in both catalogs. There are an additional 66 217 extragalactic sources that exist in WISE but not in *Gaia*. These are fit as modified blackbodies per source.

Within the Galactic plane, there are many stars per single DIRBE pixel. In order to avoid degeneracies between individual point sources, we create a map at $N_{\text{side}} = 512$ that includes all WISE point sources that are > 8 mag at 3.4 μm but have not been identified within the *Gaia* catalog. The SED's as derived by *Gaia* are then averaged over and used to scale the entire template. Within the Gibbs chain, this is sampled with a total scaling parameter, with a fixed map and relative amplitudes between different frequencies. For a full description of the star model, see the work in companion paper Galloway et al. (2024).

4.3. COBE-FIRAS

The COBE-FIRAS experiment was an absolutely calibrated differential Michelson Fourier transform interferometer that observed the full sky from 68 GHz–2911 GHz with 13.6 GHz frequency resolution (Fixsen et al. 1994; Mather et al. 1999). FIRAS's primary goal was the characterization of the CMB blackbody spectrum (Mather et al. 1994), which motivated much of the experiment's design choices. In particular, its angular resolution of 7° was chosen due to its focus on monopole characterization, while still allowing for foreground mitigation. Notably, the calibration for DIRBE and FIRAS were performed independently, although they have been compared explicitly by Fixsen et al. (1997). The possibility of improving the 140 and 240 μm bands has already been noted to reduce the discrepancy between the two experiments. The possibility of joint determination of gain and zodiacal emission using both of these datasets will be explored in future work.

Due to the observation strategy, there are non-negligible correlations between nearby frequencies, and smearing along the scanning direction, corresponding to an effectively nonsymmetric beam. In order to take the beam into account, we explicitly smooth the sky model following the same prescription as in Odegard et al. (2019) when comparing with the FIRAS bands. The dense frequency spacing of the FIRAS data makes it ideal for determining the continuum behavior of sky emission and allows for identification of emission lines (Bennett et al. 1994). To avoid the correlation between nearby bands, we used a subset of the FIRAS bands, listed in Table 2. A full comparison using the correlation between bands, similar to Bianchini & Fabbian (2022), will be performed in future analysis.

Table 2. List of FIRAS bands used in this analysis.

Frequency (GHz)	Wavelength (μm)	Purpose
108	2776	Planck 100 GHz gain monitor
149	2012	Planck 143 GHz gain monitor
217	1382	Planck 217 GHz gain monitor
353	849	Planck 353 GHz gain monitor
544	551	Planck 545 GHz gain monitor
857	350	Planck 857 GHz gain monitor
1251	240	DIRBE 240 μm gain monitor
1809	166	C II SED constraints
1890	159	C II SED constraints
1904	157	C II SED constraints
1918	156	C II SED constraints
2081	144	C II SED constraints
2135	140	DIRBE 140 μm gain monitor
2802	107	DIRBE 100 μm gain monitor

4.4. Mask definitions

In order to model the TODs accurately, we make use of processing masks depending on the band and component being modeled. In particular, estimating the instrumental noise properties and the zodiacal emission require a sufficiently accurate model, which can be easily biased in regions of excessively high emission.

For zodiacal emission, masking out the Ecliptic plane is necessary for all bands. As discussed in Sect. 7 and elaborated on in San et al. (2024), the Ecliptic plane has a complex structure that is not well fit by current parametric models. In addition, incorrectly modeled Galactic emission in the form of thermal dust and stars can bias measurements as well. As shown in Fig. 4, this mask, shown in blue, is wavelength-dependent, and is most aggressive in regions where zodiacal emission is brightest, and where point sources are brightest. Conversely, at very long and very short wavelengths, a more aggressive Galactic mask is required. These are shown in green in Fig. 4, and are defined again by regions in which the foregrounds are bright and not modeled sufficiently well.

5. Markov chains, burn-in and convergence

With the model in hand, we run Commander3 on the data. We find that an average Gibbs iteration takes approximately 500 CPU-hrs, excluding initialization time. In order to ensure proper sampling of the full distribution, we run six independent Commander3 runs initialized with their own random seeds. Each chain has 155, 157, 158, 160, 163, and 160 samples, giving a total of 953 samples. A total of one month walltime on 416 computing cores was required to produce these samples.

In order to assess burnin and convergence, we plot a range of parameters from the Gibbs chain in Fig. 5. Included in this figure are the sampled monopoles, zodiacal dust albedos and emissivities, and instrumental parameters, including the estimated white noise in bands 1 and 10, and the correlated noise parameters f_{knee} and α for band 10. From this figure, some burnin can be seen in the monopoles, concluding at approximately sample 20. At the same time, there is still drift within the emissivity and albedos, especially for parameters less strongly expressed in the model, such as $A_{4,C}$ and $E_{9/10,C}$. However, since the monopoles are stable beyond this point, this is mainly due to degeneracies within

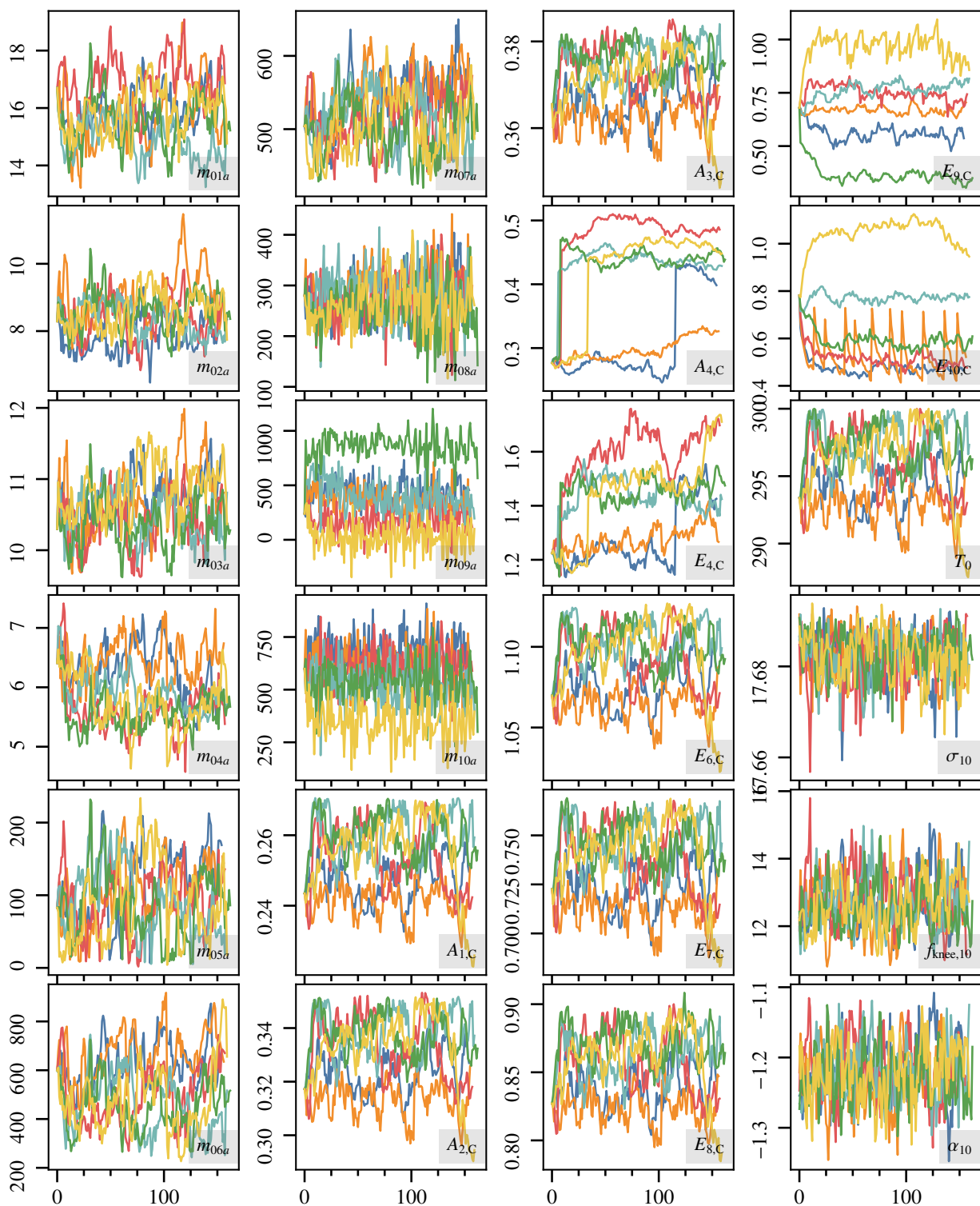


Fig. 5. Trace plots of MCMC sampling chains. Each panel shows a series of sampled components for each Gibbs sample, including the ten DIRBE monopoles, the zodiacal dust cloud albedos A and emissivities E , the ambient dust temperature at 1 AU T_0 , and the instrumental parameters for band 10. Monopoles are plotted in units of kJy sr^{-1} , $f_{\text{knee},10}$ in Hz, σ_{10} in MJy sr^{-1} , and T_0 in kelvin, while all other parameters are unitless.

the zodiacal model itself. This is explored in full detail in [San et al. \(2024\)](#).

Discarding the burnin of 20 samples, we obtain a total of 833 independent Gibbs samples. In our analysis, we truncate all chains to be the length of the shortest chain, giving a total of 810 samples. Due to the extended burn-in of the zodiacal param-

eters, individual ZL parameters cannot be considered as fully converged. However, this does not affect the monopoles and frequency maps, which only depend on the sum of all ZL components, which are the main topic in this paper.

We can also compute the correlation between parameters in the Gibbs chain, as displayed in [Fig. 6](#). As expected, there

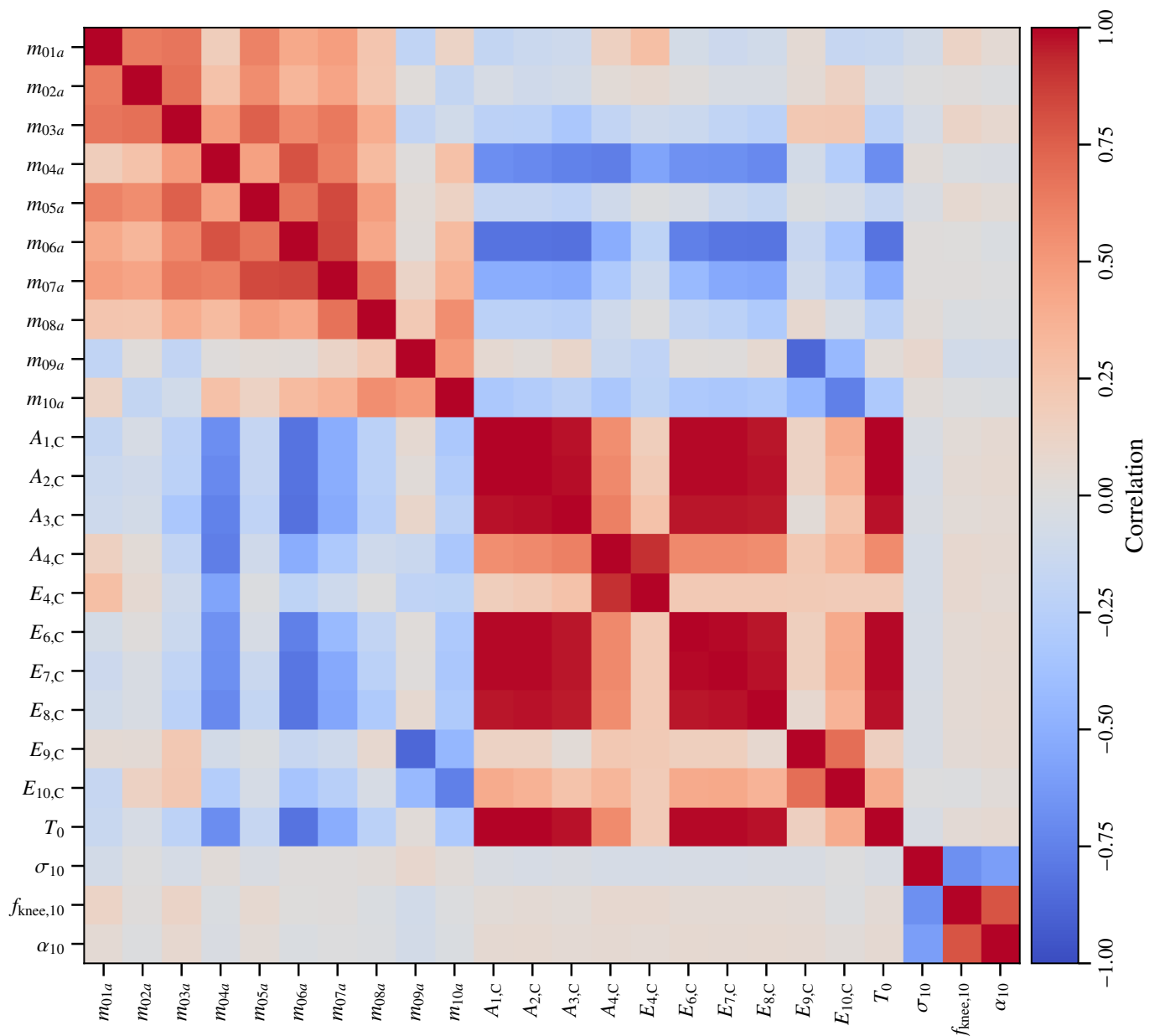


Fig. 6. Correlations between a selection of all sampled parameters. The band monopoles are denoted m , while A and E are the albedos and emissivities of the zodiacal light cloud per band, T_0 is the dust temperature, and σ_{10} , $f_{\text{knee},10}$, and α_{10} are the instrumental noise parameters in band 10, i.e., the $240\ \mu\text{m}$ channel.

are strong correlations between the zodiacal dust parameters. Likewise, there are strong correlations between monopoles of nearby frequency maps. There are small correlations, on the order of 10%, between the monopoles and zodiacal dust parameters. While these correlations are expected, the relatively low correlation indicates that the zodiacal dust and the monopole signal are relatively decoupled.

The two instrumental noise parameters are chosen as representative of the behavior of instrumental noise parameters in general. The white noise level is correlated with the monopoles and local dust temperature T_0 , demonstrating the dependence of some instrumental parameters on the final noise level. Conversely, band 10's noise parameters, while degenerate with each other as expected (see Brilenkov et al. 2023 and Ihle et al. 2023), have negligible correlation with zodiacal dust and monopole parameters.

6. Noise estimation and goodness of fit

We now turn our attention to aggregate posterior statistics, typically in the form of posterior mean and rms estimates for each sampled quantity, and we start with noise estimation and overall goodness-of-fit statistics. The algorithms used in the current analysis to estimate the instrumental noise parameters are identical to those described by Ihle et al. (2023) as applied to *Planck* LFI, and we refer the interested reader there for further details.

6.1. Instrumental noise

As defined in Sect. 2.1, ξ_n denotes the set of all instrumental noise parameters in our data model, and for all channels except $240\ \mu\text{m}$ this simply consist of a white noise rms per TOD sample, σ_0 , which is assumed to be constant within each 24 hr data seg-

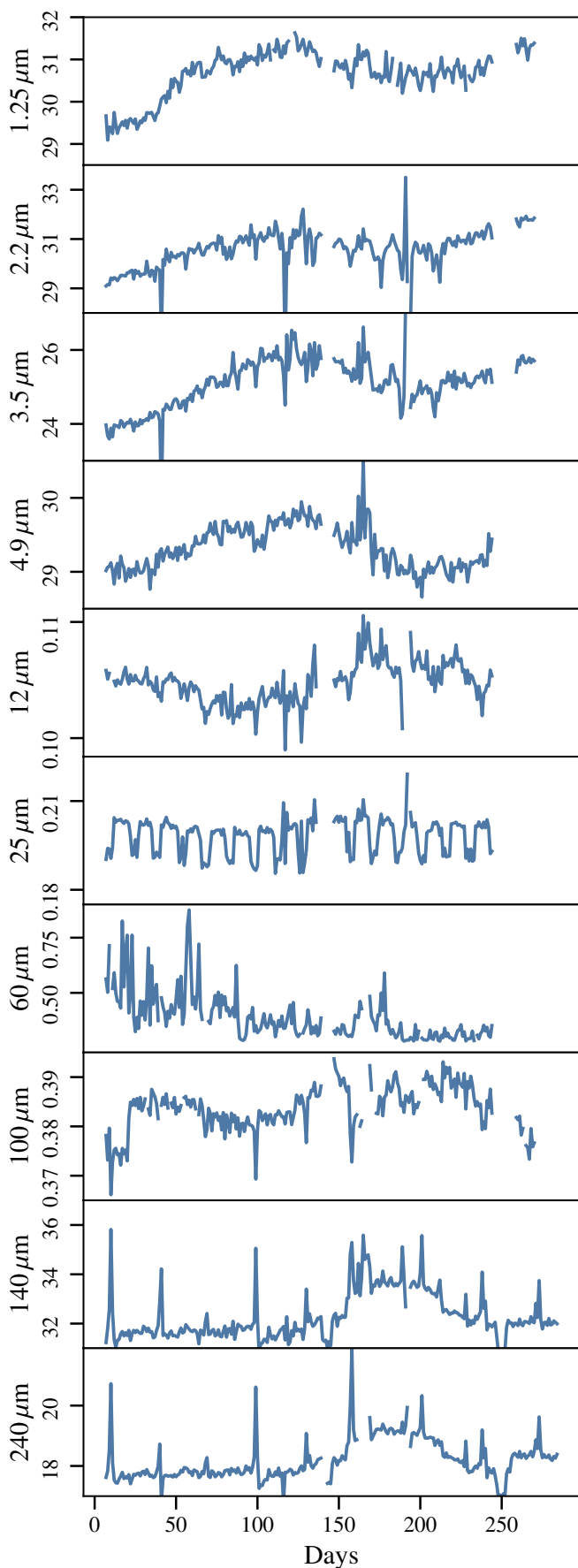


Fig. 7. Instrumental noise σ_0 for each band, averaged over all Gibbs chains. Data not used in the Gibbs chain are not displayed. Bands 12–240 μm are plotted in units of MJy sr^{-1} , while all others are in kJy sr^{-1} .

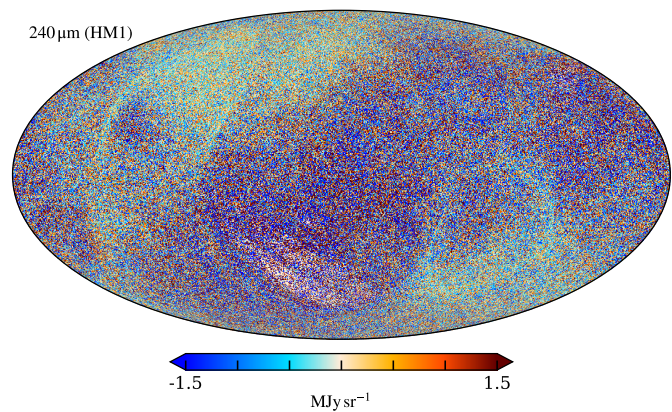


Fig. 8. Realization of correlated noise for first half-mission of 240 μm band, from the 25th sample of the first chain.

ment. The corresponding posterior mean is plotted as a function of observing day in Fig. 7. Gaps in each curve indicate observations that have been excluded from the analysis, either due to the original DIRBE data quality flags or our additional exclusion of the last two or four weeks of observations; see Sect. 3.3.

Several interesting features may be seen in this figure. Starting with the 1.25 μm channel as shown in the top panel, we notice an average increase by about 3% from the beginning to the end of the survey. This increase is however not increasing uniformly, but rather exhibits systematic variations as a function of time. Similar features are observed for all the four shortest wavelength bands, both in terms of absolute amplitude and general behaviour. Perhaps the most natural explanation for such behaviour are changes in the thermal environment of the DIRBE detectors, for instance due to varying levels of radiation from the Sun or the Earth. As demonstrated by Ihle et al. (2023) within the BEYONDPLANCK analysis by correlating σ_0 with house-keeping focal plane thermometer measurements, this was the case for *Planck* LFI. We have not yet been able to locate similar publicly available house-keeping information for DIRBE.

In contrast, the 25 μm channel exhibits a qualitatively different behaviour. In this case, σ_0 appears to jump between two different stationary states that are separated by 5% in amplitude. At one level, this general behaviour appears structurally similar to a phenomenon called “popcorn” or “random telegraph” noise, which was also observed in several *Planck* detectors, in which the noise level jumps between two discrete and well-defined levels. However, the behaviour seen in Fig. 7 appears more systematic than what is usually observed for popcorn noise, with a very well-defined period of about 2 weeks. This time scale could possibly suggest that the Moon plays a role in this behaviour, which has a rotation period relative to the Earth of about 4 weeks.

Moving on, the 60 μm channel exhibits much larger drifts than any of the others, and changes by almost 50% from the beginning to the end of the survey. We also see a clear change in the level of variations between scans as a function of the survey, with much stronger variations in the first third of the mission. In contrast, the 100 μm channel appears much more stable, and is in fact structurally quite similar to the short wavelength channels.

Finally, the 140 and 240 μm channels behave yet again differently from the other eight, with a very stable plateau during the first half of the mission, but with a clear increase around Day 180. These two channels, however, are internally very similar, and individual features and spikes can be traced very accurately between the two. In this respect, it is worth recalling the instru-

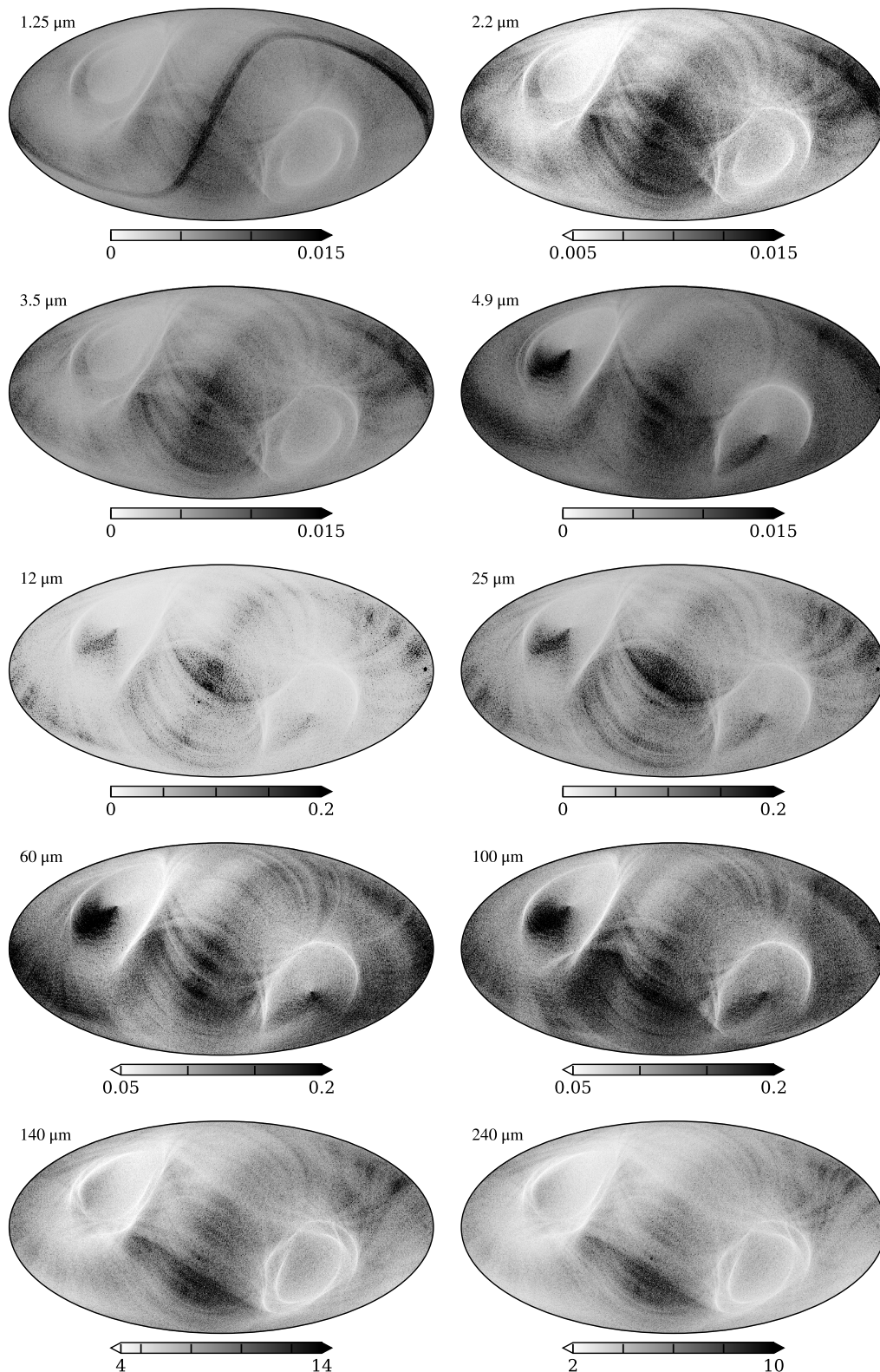


Fig. 9. White noise rms maps for each DIRBE channel. All maps are in units of MJy sr^{-1} .

ment layout shown in Fig. 1, where we see that these two channels are co-located in the optical path, separated from the others. It is therefore plausible that these two detectors experience a different thermal environment than the others.

Even more notable than the time variations in the 140 and 240 μm channels are their much higher overall noise level, which

is almost two orders of magnitude higher than for the other channels. This is due to the different detector technology used for these two channels (Hauser et al. 1998). This also implies that these channels are where the instrumental noise is best understood, allowing for a correlated noise PSD as well as noise realizations to be fit and removed in the 240 μm band. One real-

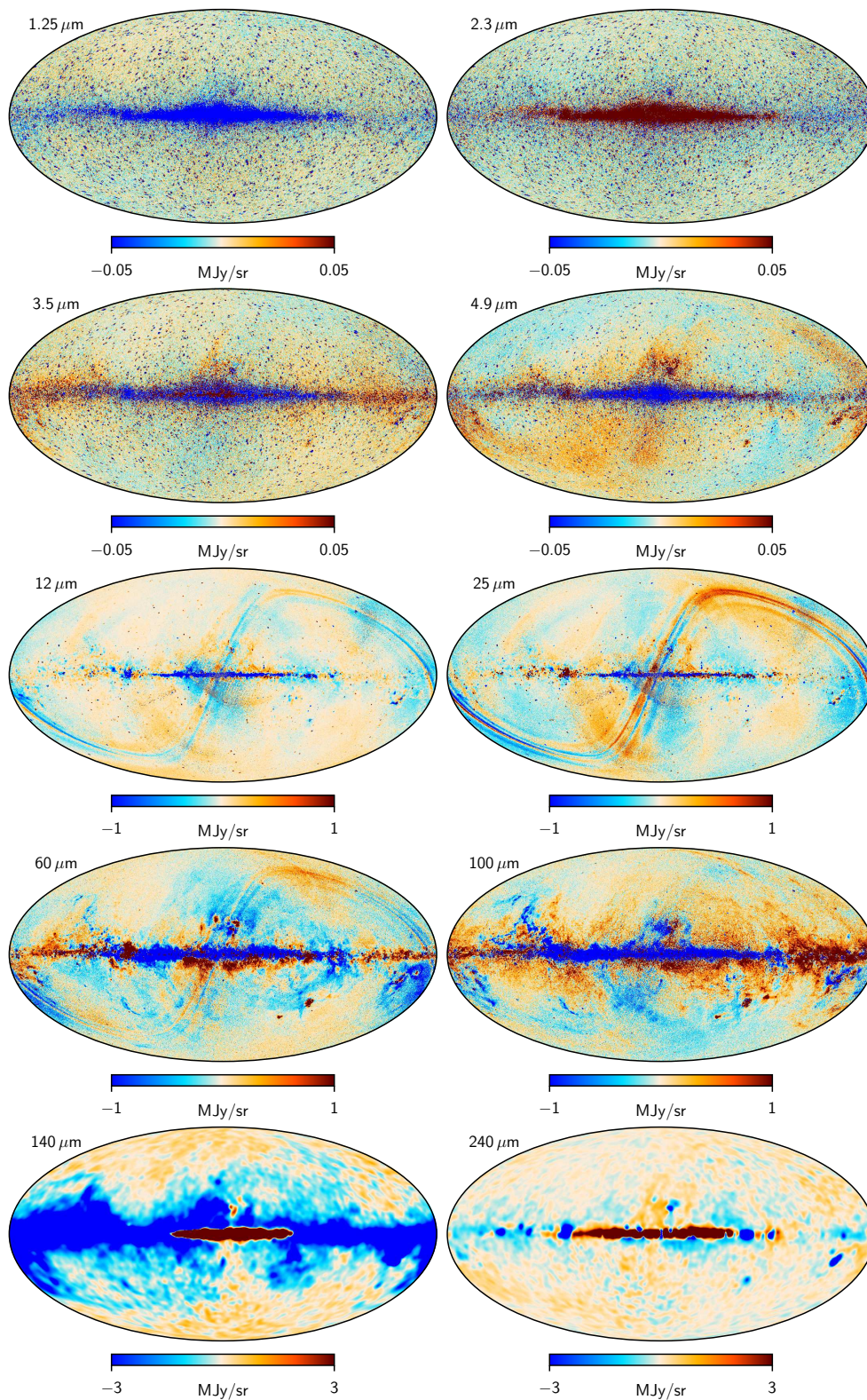


Fig. 10. Data-minus-model residual maps for each band for one arbitrarily chosen Gibbs sample. The 140 and 240 μm channels have been smoothed to an angular resolution of 3° , while all others are shown at their native resolution.

ization of this correlated noise map is shown for the first half-mission split in Fig. 8. Given that this map is derived directly from the signal-subtracted frequency map, and therefore essentially acts as a “trash can” for unmodelled effects, the absence of large coherent features provides strong evidence that the adopted signal model is indeed able to account for all main effects.

While Fig. 7 shows the white noise level in time-domain, Fig. 9 shows the corresponding noise rms as a function of position on the sky after accounting for the number of observations per pixel. Starting once again with the 1.25 μm channel, the smooth underlying variations that appear nearly symmetric with respect to the Ecliptic poles are simply due to the DIRBE

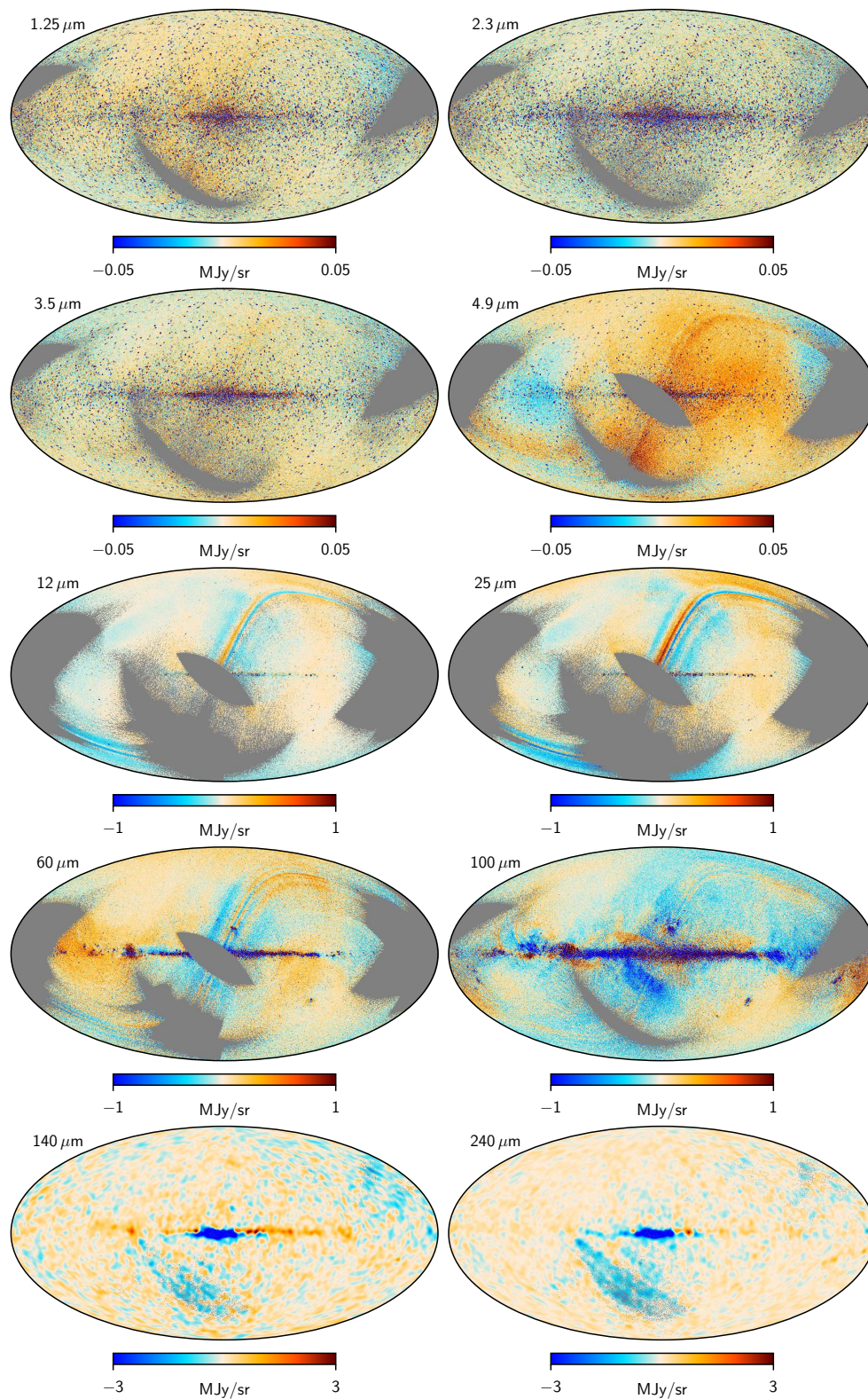


Fig. 11. Zodi-subtracted half-mission half-difference maps for each channel for one arbitrarily chosen Gibbs sample. The 140 and 240 μm channels have been smoothed to an angular resolution of 3° , while all others are shown at their native resolution.

scanning strategy, which effectively observe the Ecliptic poles more often than the Ecliptic plane. The sharp band of higher values along the Ecliptic plane is however not due to the scanning strategy as such, but rather by the DIRBE quality flags which removes near-planet observations. The 2.2 and 3.5 μm channels show very similar behaviour.

In general, the patterns seen in the 4.9–60 μm channels also appear broadly similar. However, in this case we can also see regions with higher noise levels near the Ecliptic poles and south of the Galactic center. These are primarily due to the excess radiation masks defined in Sect. 7, which removes a significant fraction of the overall data, and affects some parts of the sky more

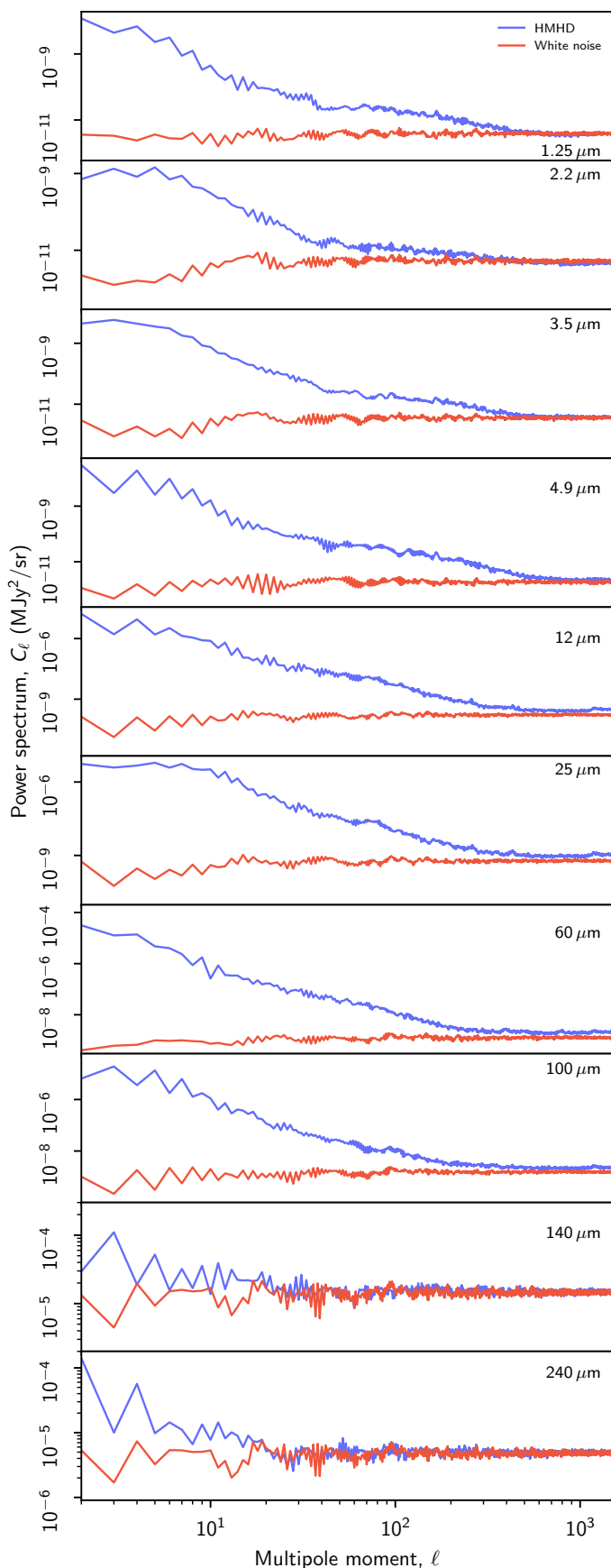


Fig. 12. Half-mission half-difference angular power spectra (blue curves) for each DIRBE channel computed with the CIB monopole masks defined by Watts et al. (2024). The red curves show the power spectrum computed from one white noise realization with the same mask.

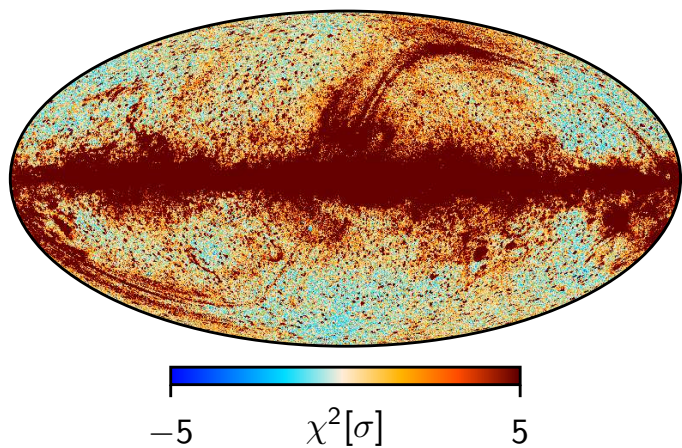


Fig. 13. Pixel-space reduced normalized χ^2 in units of σ . The number of degrees-of-freedom per pixel is here assumed to be 103, which is equal to the sum of the number of observations per $N_{\text{side}} = 512$ pixel minus the number of freely fitted Galactic components.

than others, depending on the specific orientation of the satellite at any given time with respect to the Sun.

6.2. Goodness of fit

With basic noise statistics in hand, we are ready to consider the overall goodness of fit of the model. The first such quality measure we consider are simply the data-minus-model residual maps for each wavelength band, and these are shown in Fig. 10. Starting from the top, we first note that the color scale range spans 50 kJy sr^{-1} , while the natural plotting scale for the full sky signal of this channel is typically 10 MJy sr^{-1} . As such, the model accounts for about 99% of the total sky signal at high Galactic latitudes. The same holds true for most other channels as well.

The dominant residual at short wavelengths is due to residual starlight emission in the Galactic disk. At $1.25 \mu\text{m}$ the starlight emission is slightly over-subtracted, while at $2.2 \mu\text{m}$ it is slightly under-subtracted. In this respect it is important to note that the starlight model presented by Galloway et al. (2024) is based on the WISE catalog, which includes about 747 million sources. While this is a large number, it is still much lower than the total number of stars in the Milky Way, which is about 100 billion. The completeness of the WISE catalog is, however, much higher at high Galactic latitudes than in the central bulge, and it is therefore not surprising that the model is not statistically adequate at low Galactic latitudes.

In general, only very faint ZL residuals are seen in the two shortest wavelength bands. In order to suppress these further, it is worth considering fitting the albedo of the asteroidal bands independently from the cloud; however, the signal-to-noise ratio of the bands at these wavelengths is very low, and there is a significant risk of introducing strong degeneracies with the starlight model by doing so.

Significantly stronger ZL residuals are seen in the 3.5 to $60 \mu\text{m}$ channels, but still at the sub-percent level of the total intensity. The asteroidal bands are particularly noteworthy at $25 \mu\text{m}$. In order to improve on these, higher angular resolution would be extremely useful, and a future joint analysis with IRAS and/or AKARI should prove useful in reducing these residuals further.

Between 60 and $140 \mu\text{m}$, the dominant residuals are clearly due to Galactic dust emission, and to improve on these, a more

detailed thermal dust model should be established. In this respect, it is worth recalling that we currently only fit two degrees of freedom per pixel for thermal dust emission from 100 GHz to 1.25 μm , and there are therefore massive opportunities for refining the current model without compromising the overall signal-to-noise ratio and introducing uncontrollable degeneracies. Natural next steps are to allow for spatial variations in the spectral parameters for each thermal dust component, as well as to subdivide the nearby dust component into more local clouds (Gjerløw et al. 2024a).

Next, Fig. 11 shows zodi-subtracted half-mission half-difference (HMHD) maps for each channel. These maps quantify seasonal variations in the overall residuals, and put strong limits both on errors in the assumed DIRBE-based calibration and in the overall ZL model. In particular, we note that the Galactic plane is only barely visible in any of these channels, and that indicates the DIRBE calibration is accurate to much better than 1% throughout the entire mission. Rather, the dominant spatial structures in these maps appear to be zodiacal in nature, with patterns matching those expected from convolving the ZL model with the DIRBE scanning strategy.

Figure 12 shows the angular power spectra computed from each of the HMHD maps as blue curves, compared with a single white noise realization from the Gibbs chain, plotted as red curves. At low multipoles, we see that the amplitude of the excess residuals typically are two orders of magnitude higher than the white noise level, which indicates that the current residuals are about one order of magnitude larger than white noise in pixel space. Above $\ell \gtrsim 100$ this discrepancy falls smoothly to about unity due to the DIRBE beam. Indeed, for the 1.25 to 3.5 and 14 to 240 μm channels, the agreement between the observed residual and the white noise model is excellent. However, for the intermediate channels between 4.9 to 60 μm there is a discrepancy of about a factor of two, and the origin of this is still under investigation.

Finally, Fig. 13 shows the total reduced and normalized χ^2 as a function of pixel on the sky in units of σ ; for an exact definition, see Basyrov et al. (2023). The number of degrees of freedom per pixel is here assumed to be 103, which equals the total number of individual frequency map pixels per $N_{\text{side}} = 512$ pixel (which is not equal to the number of data channels, because the *Planck* bands have higher resolution than DIRBE) minus the number of diffuse components. In this figure, we clearly see both the Galactic and ZL residuals, as discussed above. However, there are also large extended regions for which the goodness of fit is within the expected range of $\pm 2\sigma$. This is a strong testament to the overall quality of the data model defined by Eq. (1). For cosmological analyses of these data, the χ^2 map in Fig. 13 serves as a useful starting point for mask definitions.

7. Excess radiation model

One of the key novel features of the current analysis is the inclusion of s_{static} in Eq. (1). This component is designed to account for excess radiation that appears static in solar-centric coordinates. The existence of such radiation was already noted by Reach et al. (1995) and Leinert et al. (1998), but never systematically characterized or corrected for in the final DIRBE data processing.

As described in Sect. 2, we model any potential excess radiation in the current analysis by subtracting all other components from the raw TOD, and bin the residual TOD into solar-centric coordinates. Because of this coordinate transformation,

the resulting component is not degenerate with most other components, but only those that actually appear static in the Earth-Sun coordinate system. In the current model, that applies only to two components in the K98 ZL model, namely the so-called circumsolar ring and the Earth-trailing feature (Kelsall et al. 1998). These two physical interplanetary dust (IPD) components are trapped in the Earth's gravitational field, and follow the Earth's annual motion around the Sun. As such, they appear to be static on the sky as seen from the Earth, and they are therefore also fully degenerate with a_{static} . For this reason, we make no attempt to refit those two ZL components in the current analysis, but rather fix the corresponding parameters at the respective K98 values. As a result, a_{static} captures any excess radiation beyond what is described by the K98 model.

7.1. Characterization

In order to characterize the spatial morphology of a_{static} as a function of wavelength, we produced a preliminary Gibbs chain as described by Eqs. (6)–(10) prior to the main production run, while imposing no constraints on the effective sky coverage of a_{static} . The main results from this calculation are summarized in Fig. 14 in terms of posterior mean maps for each channel. Blue pixels corresponds to directions on the sky that are never observed by the DIRBE instrument, while the thin gray line corresponds to the edge of a set of processing masks discussed further below. Each of these maps is thus the full residual signal in the DIRBE data that is not captured by the assumed ZL and astrophysical parametric model, binned into solar-centric coordinates.

Browsing through the various panels, we can immediately make several interesting observations. First, we see that the two channels in the bottom row, i.e., the 140 and 240 μm channels, appear for all practical purposes consistent with instrumental Gaussian noise. There are no signatures of any excess radiation in these channels, and that is a strong testament to the efficacy of the current model at long wavelengths.

The same also holds true to a large extent at the three shortest wavelengths between 1.25 and 3.5 μm . For these, most of the sky does indeed appear to be dominated by noise, with three notable exceptions. First, at low solar elongations e – that is, pixels that lie close to the center – one may see a slight positive and circular excess along the boundary of the observed region. Second, there are clear features with both positive and negative signs aligned with equator, i.e., the Ecliptic plane. Finally, there is a faint signature of large-scale features even at high Ecliptic latitudes, in particular in the 3.5 μm channel.

However, this general picture appears quite different at the intermediate wavelengths between 4.9 and 60 μm . For each of these, an excess radiation is measured with very high signal-to-noise ratio. The most striking example is the 25 μm channel, for which the instrumental noise is fully sub-dominant.

When interpreting these maps physically, it is important to note that any model error in the Galactic foreground model will turn into horizontal stripes in these coordinates, due to the DIRBE's annual motion around the Sun. In the current set of plots, this is most clearly seen in the 100 μm channel, for which several stripes are clearly visible; these are most likely due to Galactic thermal dust residuals. Conversely, the strong signal observed at 25 μm cannot be explained in terms of Galactic residuals.

One possible hypothesis that could explain this signal is a yet unknown, and unmodelled, IPD component, fully analogous to the circumsolar ring and Earth-trailing feature. Indeed, Leinert

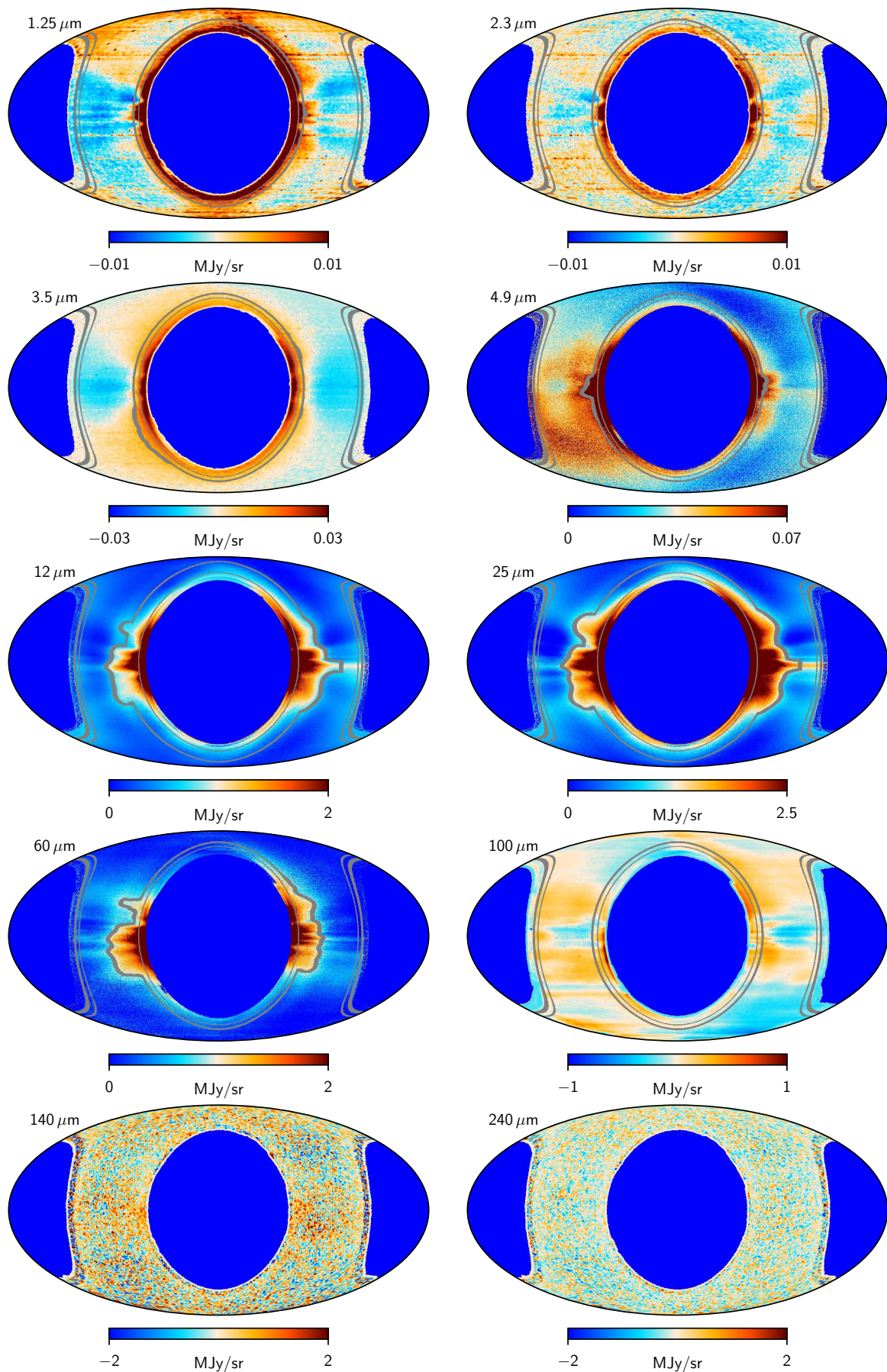


Fig. 14. Solar-centric residual maps, derived by co-adding the residual TOD, $r = d - s_{\text{fg}} - s_{\text{zodi}} - n_{\text{corr}}$, into solar-centric coordinates. The Sun is located in the center of each panel, and the equator is aligned with the Ecliptic plane. All maps have been smoothed with a 1° FWHM Gaussian kernel. The gray boundaries indicate the solar-centric exclusion masks used for each channel; no masks are applied for 140 and $240 \mu\text{m}$.

Table 3. Key map-level characteristics of the COSMOGLOBE DR2 ZSMA maps. The relative calibration, α , is defined as the slope of a scatter plot between the old K98 and new DR2 maps, evaluated over either the default DR2 processing mask (“High latitudes”) or full sky.

CHANNEL ID	BANDPASS ^(a)			RELATIVE CALIBRATION, α		NOISE RMS ($\kappa\text{Jy sr}^{-1}$) ^(b)	
	ν_c (THz)	λ_c (μm)	$\Delta\nu/\nu$	High lat	Full sky	K98	DR2
1	240	1.25	0.25	1.025	1.068	1.0	1.3
2	136	2.2	0.16	1.022	1.034	1.2	1.8
3	85.7	3.5	0.26	1.012	1.031	1.1	1.5
4	61.2	4.9	0.13	0.974	1.028	1.3	1.3
5	25.0	12	0.53	0.629	0.943	3.6	8.8
6	12.0	25	0.34	0.206	1.019	7.5	15
7	5.00	60	0.46	1.009	0.988	18	18
8	3.00	100	0.32	1.005	1.041	17	19
9	2.14	140	0.28	0.784	1.013	1530	1270
10	1.25	240	0.40	0.841	1.012	860	740

^a Reproduced from the DIRBE Explanatory Supplement.

^b Noise sensitivity per $0.7^\circ \times 0.7^\circ$ pixel, averaged over the full sky.

et al. (1998) refer to all the observed radiation simply as “excess zodiacal light brightness due to the resonant dust ring outside the Earth’s orbit”. However, that characterization was based on a visualization that still included the circumsolar ring and trailing feature contributions. In our maps, however, those contributions are already subtracted, and the signals that we observe in Fig. 14 must therefore be due to unmodelled components.

Considering the $25\mu\text{m}$ signal in greater detail, we both see a strong excess that appears nearly symmetric with respect to the Sun at low solar elongations, as well as a four-fold symmetric structure at higher solar elongations. In contrast, the $4.9\mu\text{m}$ channel exhibits a clear dipolar structure, in which the signal is clearly brighter in the lower left quadrant than in the upper right quadrant. At $60\mu\text{m}$, there is a linear structure that extends from the upper left to the bottom right quadrant. In general, it is not trivial to envision a physical IPD structure that can explain all of these structures simultaneously with reasonable assumptions regarding its SED, and more work is certainly needed in terms of IPD modelling to understand what the full set of constraints actually are.

However, there is another physical mechanism that is also worth mentioning in this respect, namely straylight or sidelobe contamination. This is a well-known problem for many, if not most, high sensitivity experiments. As discussed in Sect. 3, the DIRBE optics were specifically designed to minimize precisely such radiation. At the same time, there exists to our knowledge no physical optical ray-tracing model for the DIRBE instrument, similar to those produced with GRASP⁹ for *Planck* and *WMAP*. Given the strong excesses seen in Fig. 14, it seems well justified to establish such in the near future; either to put strong numerical limits on the amplitude of such straylight if it is indeed negligible, or to derive a model that can be used directly to subtract the emission in the case that it is non-negligible.

7.2. Mitigation through masking and subtraction

As far as the current analysis is concerned, determining the true physical origin of the excess signal is only of secondary importance, and we choose for now to remain agnostic in this respect. The key point at this stage, however, is to minimize its impact on the final ZSMA maps, which serve as the inputs to any DIRBE-based cosmological and astrophysical analysis. This can be done

⁹ <https://www.ticra.com/software/grasp/>

in two ways. First, one may exclude any pixel in solar-centric coordinates with particularly strong excess. This is similar to the approach taken by Kelsall et al. (1998); while they did not produce detailed maps like those in Fig. 14, they plotted residuals as a function of solar elongations, and noted that particular strong excesses were seen for $e < 68^\circ$ and $e > 120^\circ$, and all those data were therefore excluded from the co-added ZSMA maps. Those limits correspond to two concentric circles centered on the Sun in Fig. 14. Secondly, for pixels that are only mildly affected by the excess, we use $\mathbf{a}_{\text{static}}$ as a template, and subtract it from the TOD prior to mapmaking, as indicated in Eq. (1).

The solar-centric masks used in the current analysis are shown as thick gray lines in Fig. 14. These were generated by thresholding each excess maps after smoothing to 3° FWHM. In addition, a sharp cut in solar elongation with varying thresholds were applied for each channel, similar to the K98 approach. For comparison, the thin gray lines show the static solar elongation limits used in the K98 analysis, and the excess signals seen between the thin and thick lines are thus contamination that is entirely eliminated in the current analysis, but still present in the official DIRBE maps.

While these masks eliminate the worst affected data, highly significant excess radiation may still be seen in the unmasked region for the $4.9\text{--}60\mu\text{m}$ channels. For these four channels we let s_{static} be non-zero in Eq. (1), while for the other six channels we set s_{static} to zero, and only apply the above masking procedure.

7.3. Zero-level determination

A side effect of applying a non-zero s_{static} correction is that the CIB monopole effectively becomes unmeasurable at the corresponding frequencies; see Watts et al. (2024). The reason for this is simply that $\mathbf{a}_{\text{static}}$ is fitted freely pixel-by-pixel, and any residual monopole that may remain in $\mathbf{r}_{\text{static}}$ will propagate directly into $\mathbf{a}_{\text{static}}$. Conversely, any monopole error in $\mathbf{a}_{\text{static}}$ will propagate directly into m_ν in Eq. (1) – and those parameters are the CIB monopole tracers in this analysis. This degeneracy is the main reason for not applying the s_{static} corrections to the $1.25\text{--}3.5$ and $100\text{--}240\mu\text{m}$ maps.

However, the ZSMA maps are useful for many other applications than CIB monopole determination as well, and it is therefore important to determine the zero-level of $\mathbf{a}_{\text{static}}$ in a physically well-motivated manner for the corrected channels. This is a priori difficult, since we do not yet know the true physical origin of

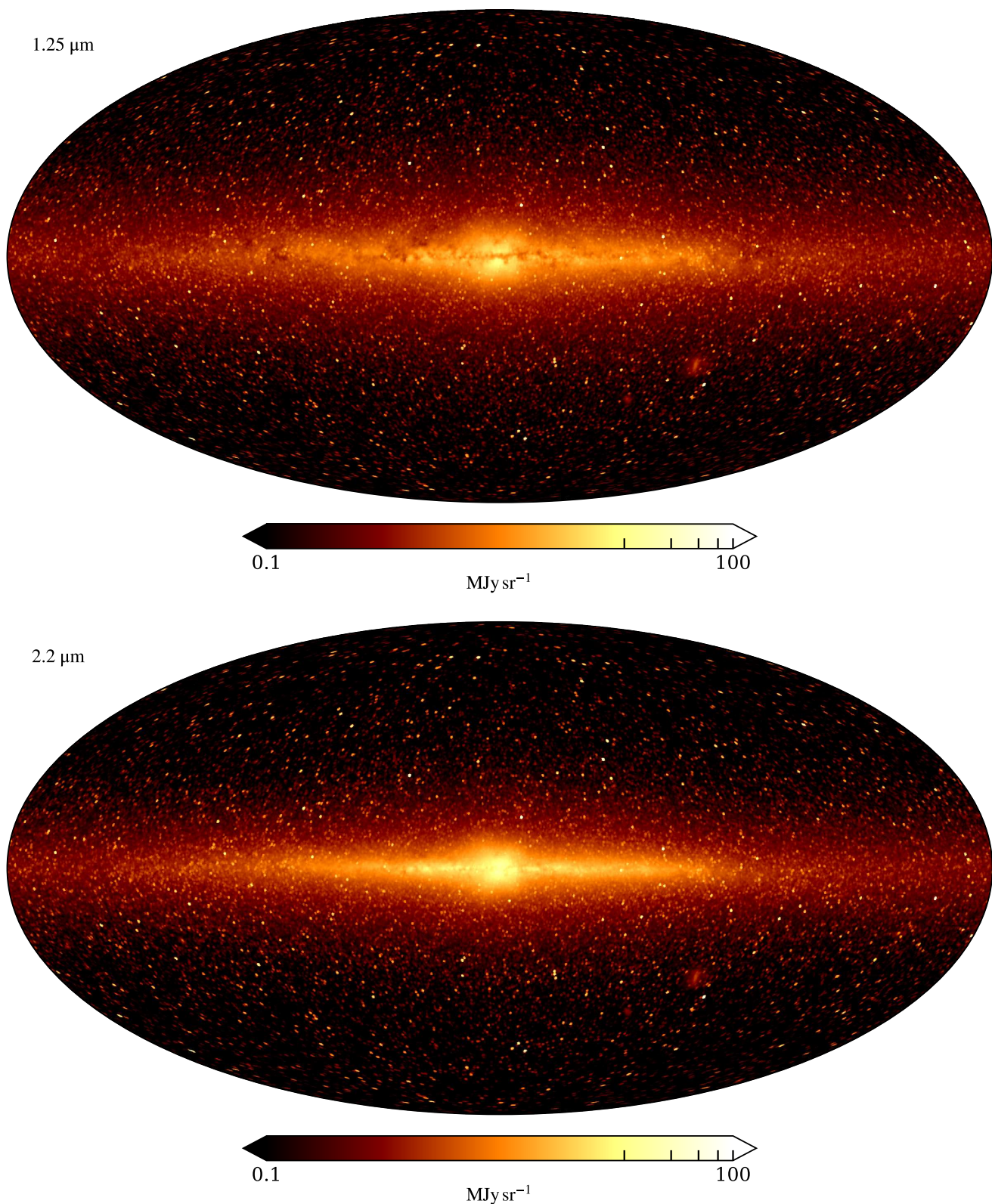


Fig. 15. COSMOGLOBE DR2 ZSMA maps at 1.25 (*top*) and 2.2 μm (*bottom*). Missing pixels have been replaced with the median of values within a 2° radius.

the signal. However, whether it is due to an unmodelled ZL component or instrumental straylight, it is reasonable to assume that the measured intensity ideally should be strictly positive. This therefore defines an absolute lower limit on the zero-level.

In practice, we set the zero-level of $\mathbf{a}_{\text{static}}$ as follows. We first smooth $\mathbf{a}_{\text{static}}$ with a Gaussian kernel of 2° FWHM to reduce the impact of instrumental noise. We then identify the lowest value in this smoothed map, and choose a value that is slightly higher

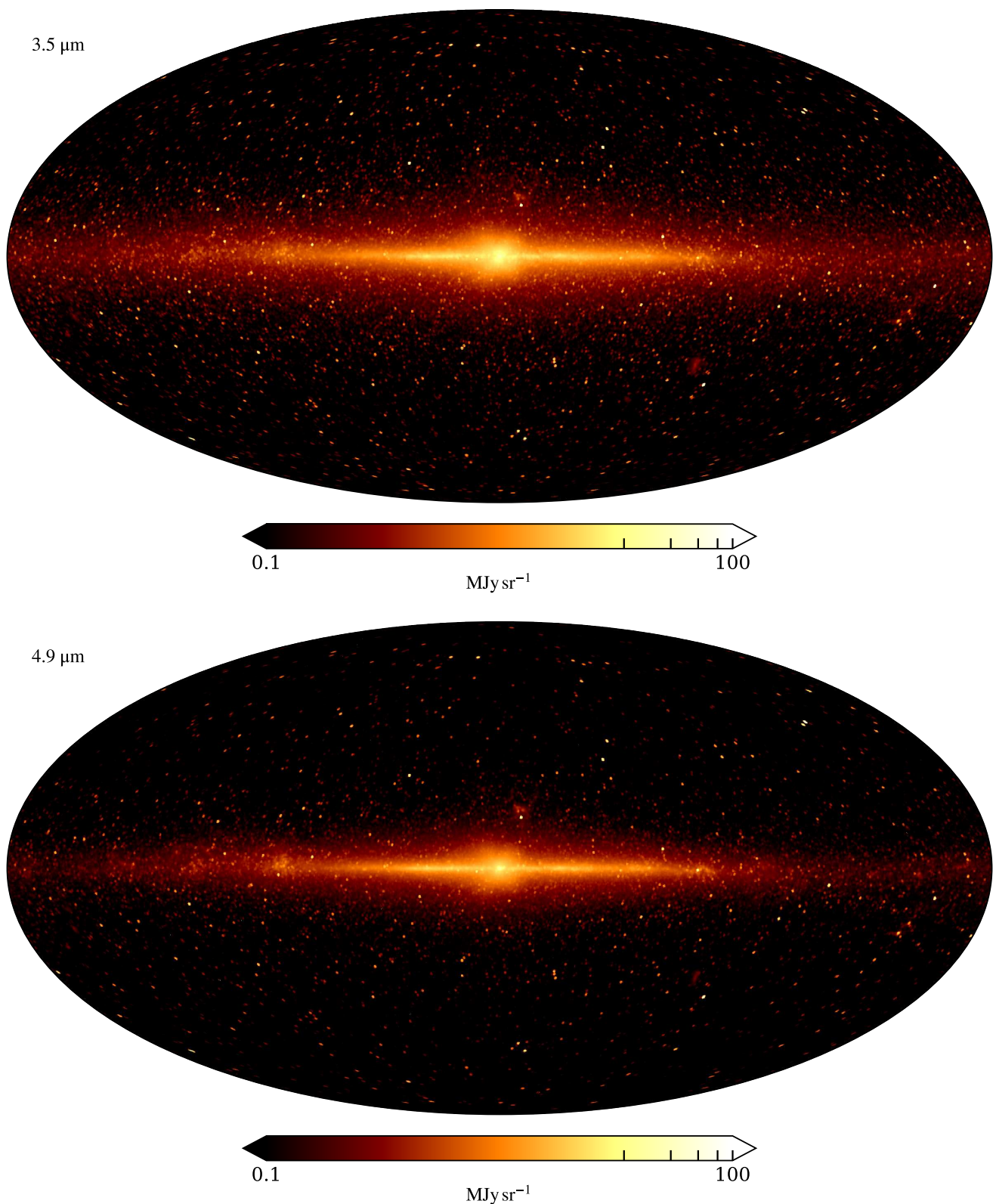


Fig. 16. COSMOGLOBE DR2 ZSMA maps at 3.5 (*top*) and 4.9 μm (*bottom*). Missing pixels have been replaced with the median of values within a 2° radius.

than this, to ensure that the value propagated into the rest of the Gibbs chain represents a physically meaningful value. We record the difference between the absolute lowest value and the final selected value, and this difference may be subtracted from the

final ZSMA maps in case an absolute lower limit is required. As discussed by [Watts et al. \(2024\)](#), this procedure provides a well-defined upper limit on a_{static} , and therefore also a well-defined upper limit on m_v , but no lower limit on a_{static} .

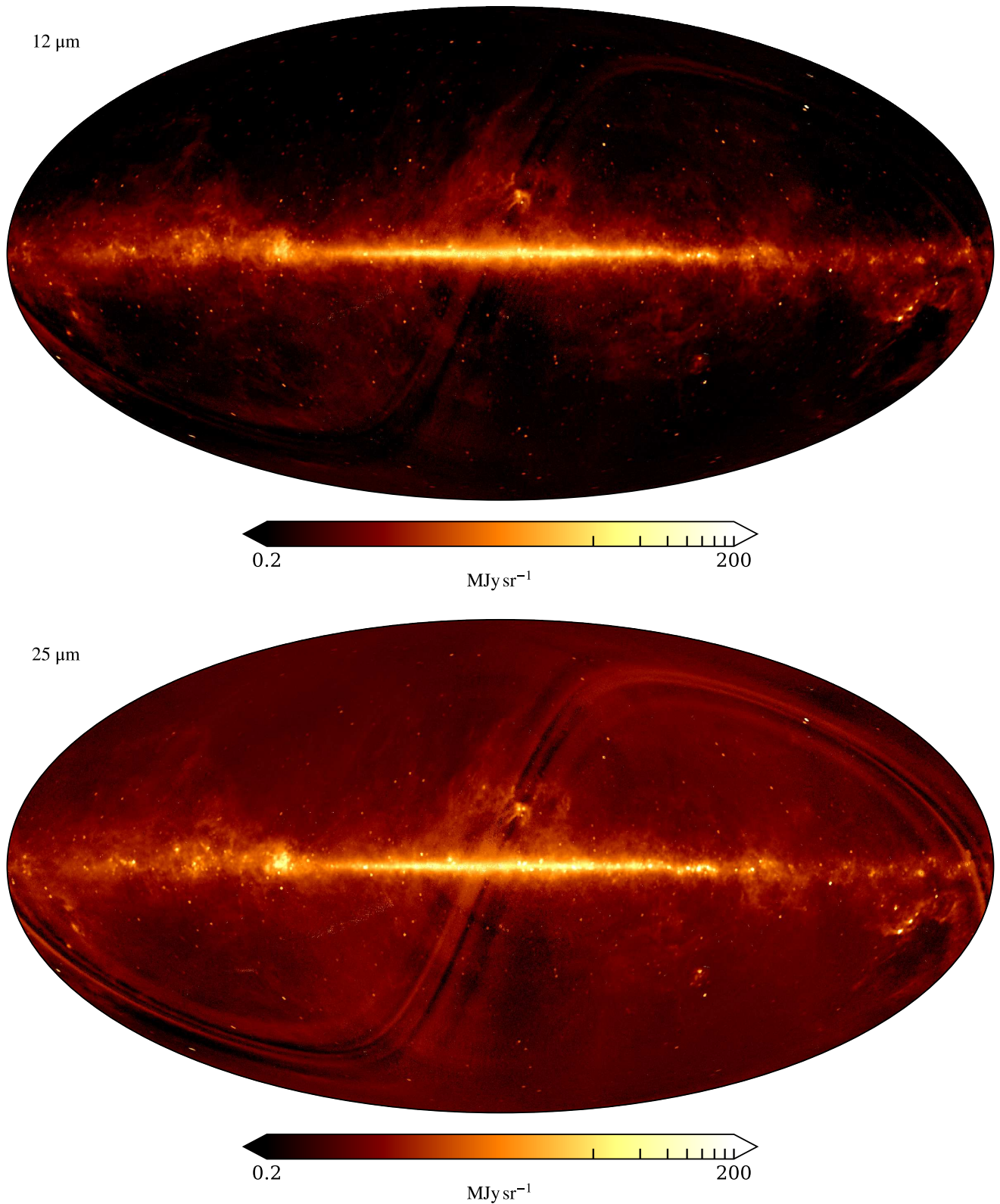


Fig. 17. COSMOGLOBE DR2 ZSMA maps at 12 (*top*) and 25 μm (*bottom*). Missing pixels have been replaced with the median of values within a 2° radius.

To estimate an uncertainty for the zero-level of a_{static} , we apply Gaussian smoothing kernels of 1, 2, 3, 4, and 5° FWHM's, and compute the standard deviation of the resulting minima. The results from these calculations, both of the corresponding uncer-

tainties are tabulated in the seventh column of Table 1 in [Watts et al. \(2024\)](#).

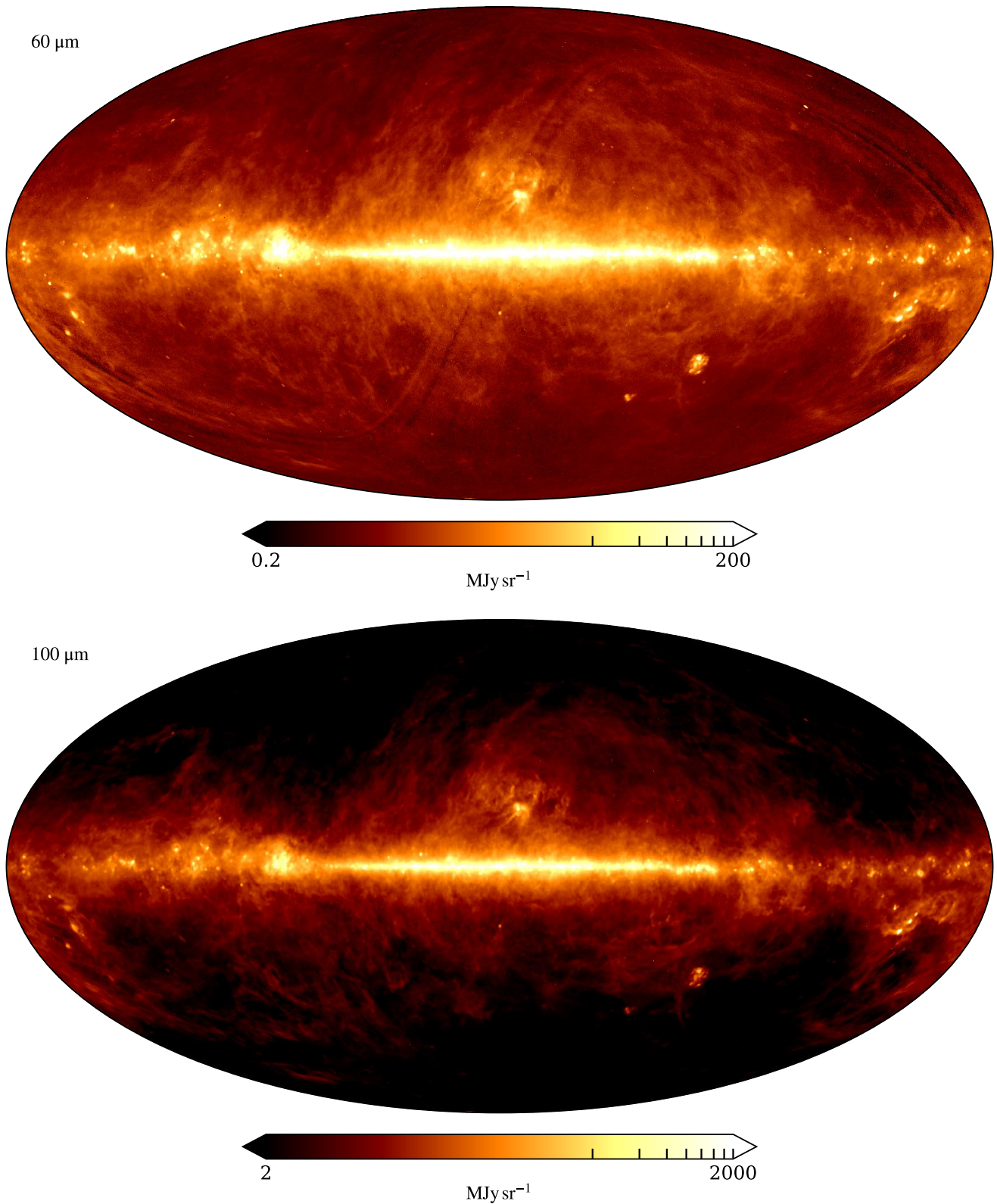


Fig. 18. COSMOGLOBE DR2 ZSMA maps at 60 (*top*) and 100 μm (*bottom*). Missing pixels have been replaced with the median of values within a 2° radius.

8. Frequency maps

We now move on to the main products in the current paper, namely the COSMOGLOBE DR2 zodiacal light subtracted mission average maps.

8.1. ZSMA frequency maps

The individual DR2 ZSMA posterior mean maps are shown in Figs. 15–19, plotted with logarithmic color scales. Browsing through these in order, we find that almost all of these appear vi-

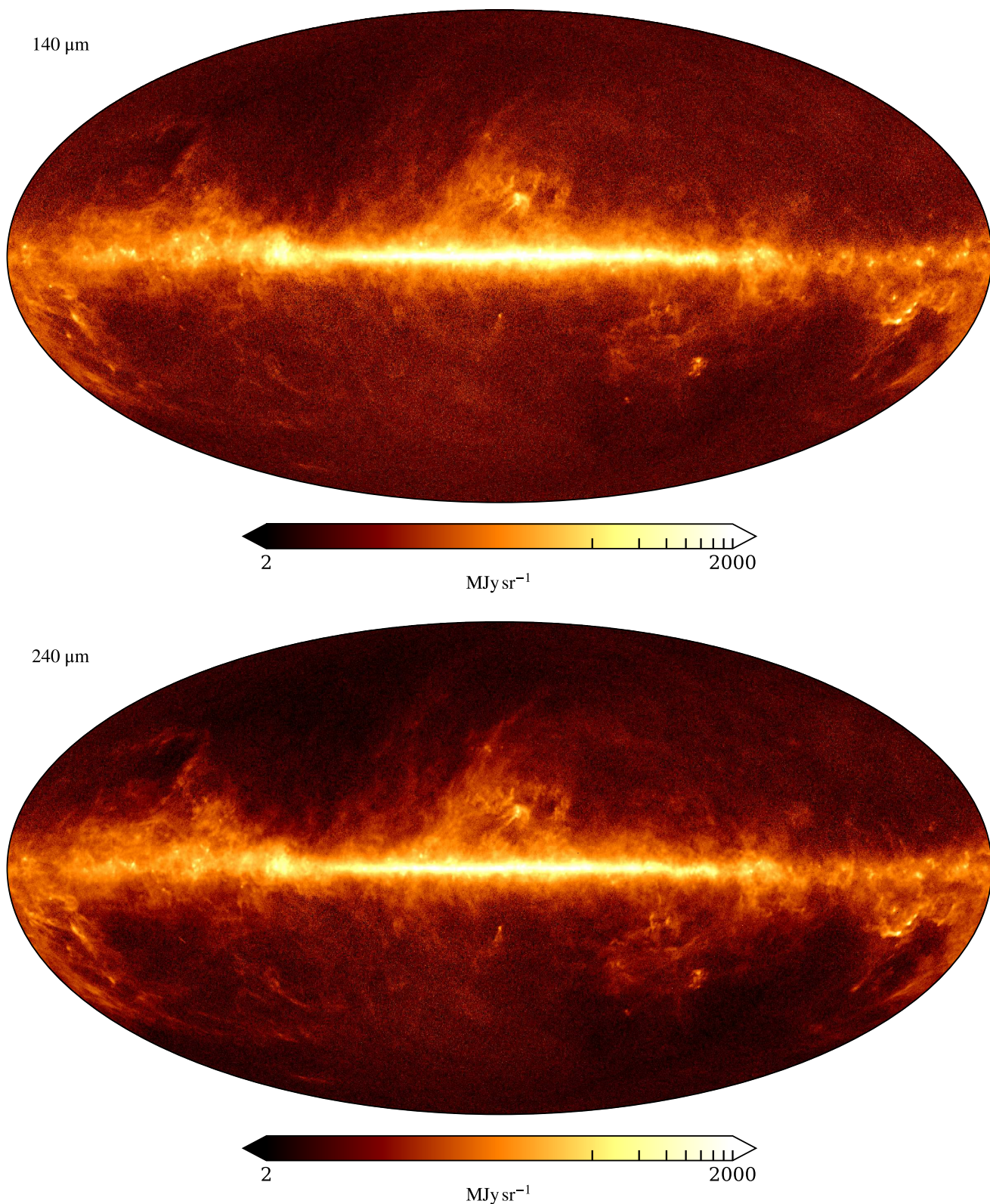


Fig. 19. COSMOGLOBE DR2 ZSMA maps at 140 (*top*) and 240 μm (*bottom*). Missing pixels have been replaced with the median of values within a 2° radius.

sually consistent with Galactic emission, and there are very few traces of residual ZL emission. However, there is one striking exception to this, namely the 25 μm channel. In this case, we see both a large residual monopole and clear ZL band residuals. A

minor exception is also the 12 and 60 μm channels, which also shows slight evidence of residual ZL band emission, although in this case the Galactic signal once again clearly dominates. In

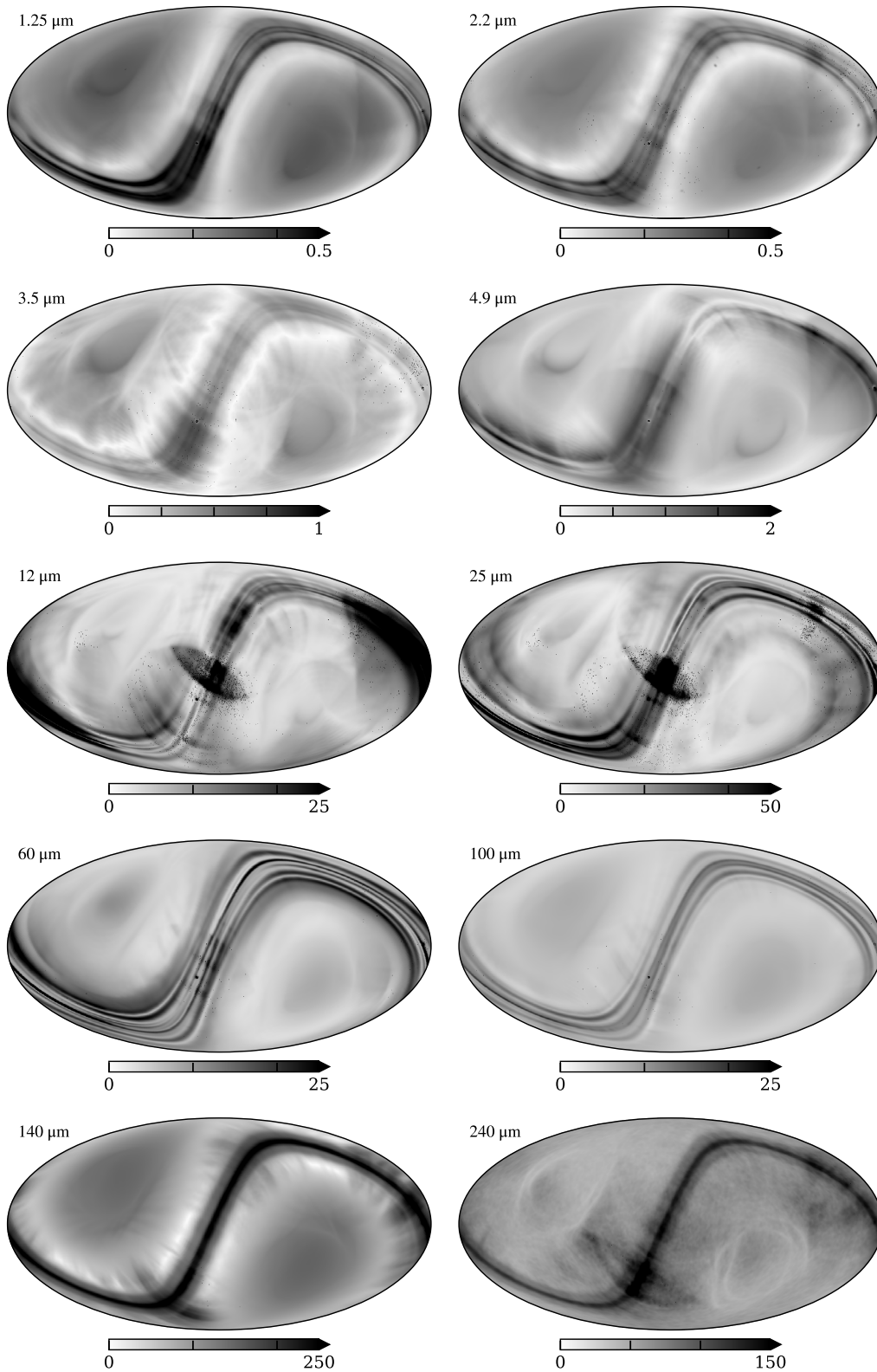


Fig. 20. Posterior rms maps for each DIRBE channel. These account for uncertainties due to model variations in each band, but not white noise. For white noise maps see Fig. 9. All maps are in units of kJy sr^{-1} .

the next section, we compare these maps with the corresponding DIRBE K98 products.

8.2. Angular power spectra

Figure 20 shows the posterior rms maps for each channel. It is important to note that these do not account for the white noise of each channel, but rather only summarize the systematic uncer-

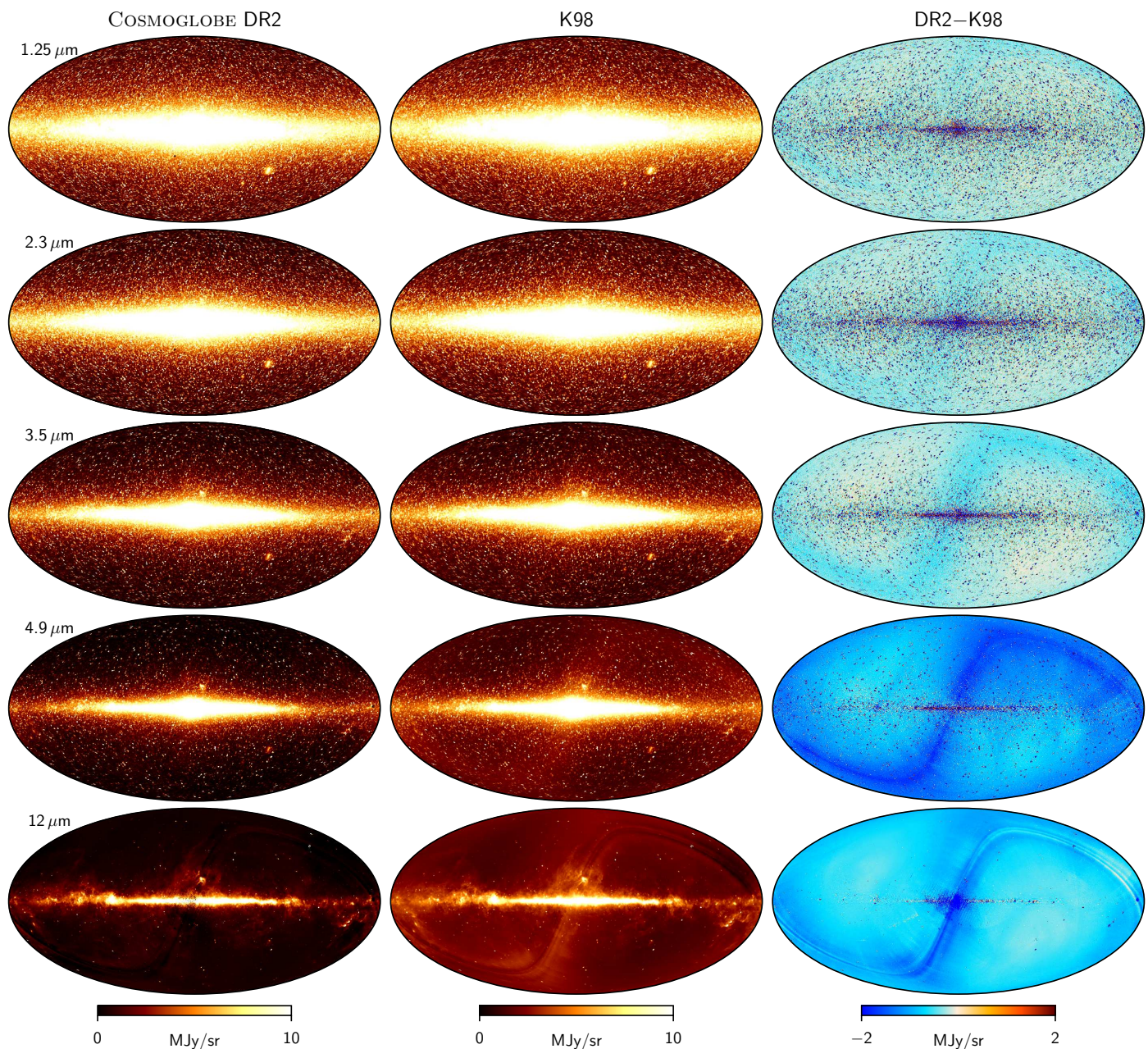


Fig. 21. Comparison of COSMOGLOBE DR2 (*left column*) and K98 (*middle column*) zodiacal light subtracted mission average maps for the 1.25 to 12 μm channels. Difference maps are shown in the rightmost column. Full maps are plotted with a non-linear color scale, while difference maps are plotted with a linear and symmetric color range.

tainties due to the other model components in Eq. (1). To obtain full uncertainties for each channel, the maps shown in Figs. 9 and 20 must be added in quadrature. However, for most scientific analyses it is better yet to analyze each individual Gibbs map sample separately, taking into account only the white noise, and then build the desired summary statistic from the ensemble of all available samples; for an example of this procedure applied to the *Planck* LFI and *WMAP* data, see, e.g., Basyrov et al. (2023), Colombo et al. (2023), Paradiso et al. (2023), Andersen et al. (2023), and Watts et al. (2023). For the 240 μm channel only, one may additionally see a low level of random noise, which is due to the correlated noise component, a single realization of which is shown in Fig. 8. The overall amplitudes of these maps are generally about one order of magnitude lower than the white noise shown in Fig. 9.

8.3. Comparison with K98

In Figs. 21 and 22 we compare the COSMOGLOBE DR2 ZSMA maps with the corresponding K98 maps as reprocessed by the CADE team; see Appendix A of Paradiso et al. (2012) for algorithmic details.¹⁰ The right column shows the difference between the two as defined by DR2–K98, so that a negative difference indicates a higher intensity in K98. Inspecting these maps channel-by-channel, we first note that the three shortest wavelength bands

¹⁰ We refer to the reprocessed CADE maps also as “K98” in the following, but note that these maps may, at least in principle, differ from the original Quadcube maps presented by Kelsall et al. (1998). In particular, we expect that the pixel remapping process used by CADE could have a non-trivial effect on the noise on small angular scales. For a general discussion of noise in so-called “drizzled” maps, see Fruchter & Hook (2002).

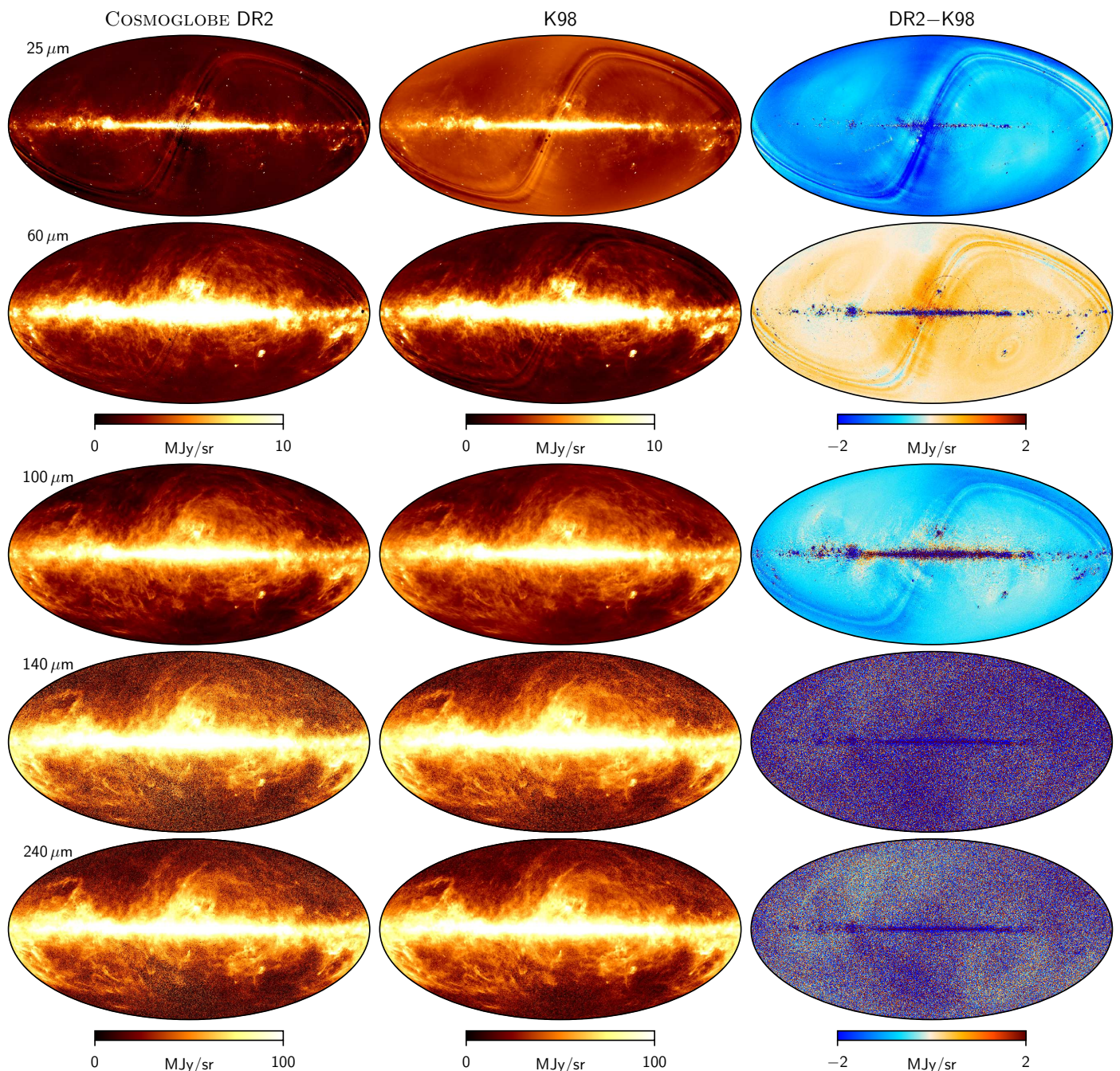


Fig. 22. Same as Fig. 21, but for the 25–240 μm channels.

appear visually very similar, and it is only through the difference map it is possible to distinguish them. Here we see that K98 has a brighter Ecliptic plane than DR2, but it is still very difficult to determine by eye which of the two reveals a cleaner Galactic signal. At 4.9 μm , however, there is no longer any visual ambiguity: Here we clearly see that the K98 map exhibits ZL residual while the DR2 model is visually clean. The same holds even more true at 12 μm .

At 25 μm , however, the relative improvements are less striking. While the DR2 map does show lower residuals than K98 also in this case, both of them are contaminated to the extent that the high-latitude regions are not useful for cosmological or astrophysical analysis. Improving this channel is a high-priority goal for future work. Similar considerations apply to the 60 μm

channel, for which our map is clearly better than K98, but faint signatures of the ZL bands are still visible.

Moving on, the 100 μm channel is particularly interesting, because the K98 map at this wavelength has served as a cornerstone for Galactic thermal dust modeling for almost three decades, and it has therefore had a massive impact in the community. By comparing the maps shown in Fig. 22, we now see clearly that the K98 version of that map contains significant ZL contamination. At high latitudes, the correction is of order unity compared to the actual Galactic signal, and it is therefore critically important to revisit previously published thermal dust emission and extinction parameters based on the K98 map. In contrast, the 140 and 240 μm channels appear very similar between the two analyses in terms of large-scale structures.

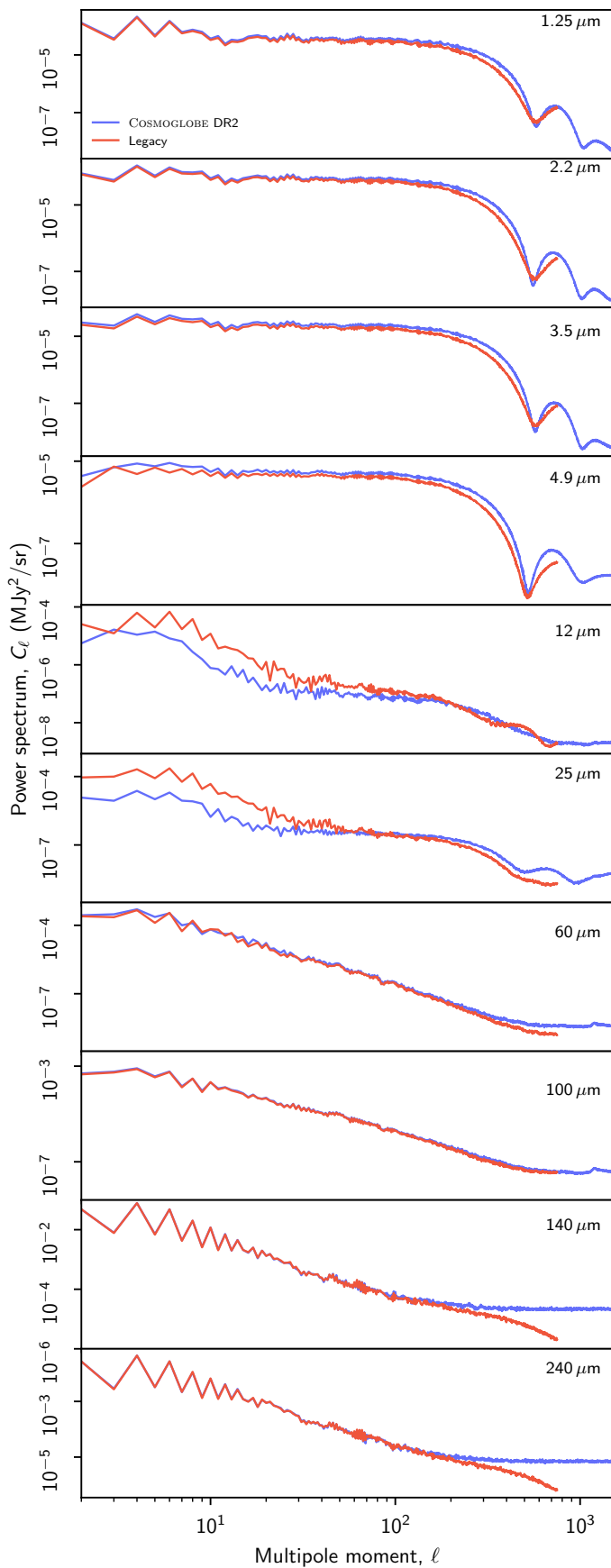


Fig. 23. Comparison of angular power spectra computed from the DIRBE (red) and DR2 (blue) ZSMA maps.

In Fig. 23 we plot the angular power spectra of both the new DR2 (blue curves) and the old K98 (red curves) as evaluated outside the DR2 processing masks. On large scales, we observe behaviour that is consistent with the above visual impression; the two map generations agree well on large angular scales for the 1.25–3.5 μm and 60–240 μm channels, while at the intermediate channels the K98 maps exhibit clear excess from ZL contamination.

However, these spectra additionally reveal notable differences on smaller angular scales. First, we see that the K98 maps exhibit lower power around the beam scale of $\ell \approx 300$. We interpret this as additional effective filtering from the coarse Quad-cube pixelization employed during the original mapmaking, coupled with the subsequent CADE repixelization into HEALPix. Second, we note that the DR2 spectra extend to twice the multipole range of those in the K98 maps, and this is due to adopting a pixelization of $N_{\text{side}} = 512$. The main motivation for this is clearly shown in the top four panels of Fig. 23. The power spectrum shows clear structure all the way up to the maximum limit of $\ell_{\text{max}} = 1500$, and this is due to bright point sources coupled with the highly non-Gaussian beam seen in Fig. 2. Despite the fact that the DIRBE resolution is only 42' FWHM, its peculiar shape requires a high pixel resolution to fully capture the full harmonic bandwidth of the signal. Indeed, from these plots it appears as though even $N_{\text{side}} = 512$ is formally sufficient, as the maps have not yet reached their white noise limit at these multipoles. The relatively coarse 8 Hz sampling rate of the DIRBE instrument implies that pixelization at $N_{\text{side}} = 1024$ would result in a large number of missing pixels, which is inconvenient to work with in practice; already with the current $N_{\text{side}} = 512$ pixelization, our maps have some missing pixels.

One final feature to note in Fig. 23 is the fact that the power spectra of the K98 maps at 140 and 240 μm show signs of additional smoothing at high multipoles. We have not been able to conclusively identify the source of this effect, but users of the K98 maps should be aware of this additional smoothing.

We conclude this section by comparing the overall relative calibration, α , of the DR2 and K98 maps, as defined by the slope of scatter plots between the two maps, evaluated either outside the DR2 processing mask (Fig. 4) or the full sky. The results from these calculations are tabulated in the fifth and sixth columns of Table 3. As evaluated over the full sky, we see that the overall calibration of the two maps agree to a few percent for most channels, and our maps are generally slightly brighter. Again, we interpret this difference as the effect of the coarser pixelization used for the K98 maps.

When considering high latitudes only, the best-fit slope differs significantly from unity, and ranges between $\alpha = 0.48$ and 1.11. This clearly illustrates the relative importance of the new maps in terms of cosmological and astrophysical interpretation at high latitudes; the improvements made in the current analysis are of order unity in the low foreground regions of the sky.

For completeness, the two rightmost columns in Table 3 compare the average instrumental noise levels of the two analyses, in which the K98 values are adopted from Table 1 of Hauser et al. (1998). In general, the two estimates agree well, given the large algorithmic differences adopted by the two analyses.

9. Conclusions

In this work, we have presented a joint analysis of DIRBE CIOs in a global Bayesian framework using external *Planck*, *Gaia*, WISE, and FIRAS data. In combination with an improved zodiacal dust model (San et al. 2024), an improved thermal dust model

(Gjerløw et al. 2024a), and an infrared stellar model (Galloway et al. 2024), we have produced maps using DIRBE data with unprecedented zodiacal dust removal and absolute monopole determination. As shown in Watts et al. (2024), these have led to improved CIB monopole constraints across all existing DIRBE bands.

While part of this improvement comes from improved compute resources, the vast majority of the processing improvement comes from complementary datasets used in this analysis. The use of *Planck* HFI and FIRAS data enabled the use of a thermal dust model that allowed for the unique features of the DIRBE data to shine through. Similar use of *Gaia* and WISE data for near-infrared point source characterization allowed for robust determination of the monopole within the DIRBE bands as well. Together, this sky model allowed for DIRBE's unique zodiacal dust and monopole sensitivity to be fully utilized.

An especially prominent feature that was noted in the data was the discovery of excess radiation in solar-centric coordinates that cannot be modeled using existing models of zodiacal dust or Milky Way emission. While part of this emission could be attributed to poorly modeled zodiacal emission, the possibility of unmodeled straylight cannot be discounted. With the currently existing data, it is not possible to determine whether this excess radiation is from an astrophysical source or straylight, and investigating this should be a high priority for a future DIRBE analysis.

A major outcome of this work is the renewed possibility of using the DIRBE maps in the analysis of CMB experiments. As demonstrated here, it is possible to create a sky model that takes into account both high-resolution *Planck* maps and the high-frequency DIRBE maps, provided that proper low-level TOD processing is included in the modeling. The fidelity of the DIRBE maps produced in this work will be indispensable for future analysis of *Planck* HFI data, providing critical information about thermal dust and zodiacal light that cannot be constrained with *Planck* alone.

At the same time, this work demonstrates the need for more external data with complementary observing strategies. The existing IRAS and AKARI maps each have much higher resolution than DIRBE with bandpasses that overlap the brightest zodiacal emission bands. An analysis taking into account all of these data at the time-ordered level will both improve the instrument characterization for all of these experiments and improve the characterization of the infrared sky. In particular, the many lines of sight across several decades will allow for the most precise model of zodiacal dust possible, while giving an as-of-yet unattainable view into the CIB.

Acknowledgements. We thank Tony Banday, Johannes Eskilt, Dale Fixsen, Ken Ganga, Paul Goldsmith, Shuji Matsuura, Sven Wedemeyer, and Janet Weiland for useful suggestions and guidance. The current work has received funding from the European Union's Horizon 2020 research and innovation programme under grant agreement numbers 819478 (ERC; COSMOGLOBE), 772253 (ERC; BIRSCOSMOLOGY), and 101007633 (MSCA; CMBINFLATE). Some of the results in this paper have been derived using healpy (Zonca et al. 2019) and the HEALPix (Górski et al. 2005) packages. We acknowledge the use of the Legacy Archive for Microwave Background Data Analysis (LAMBDA), part of the High Energy Astrophysics Science Archive Center (HEASARC). HEASARC/LAMBDA is a service of the Astrophysics Science Division at the NASA Goddard Space Flight Center. This publication makes use of data products from the Wide-field Infrared Survey Explorer, which is a joint project of the University of California, Los Angeles, and the Jet Propulsion Laboratory/California Institute of Technology, funded by the National Aeronautics and Space Administration. This work has made use of data from the European Space Agency (ESA) mission *Gaia* (<https://www.cosmos.esa.int/gaia>), processed by the *Gaia* Data Processing and Analysis Consortium (DPAC, <https://www.cosmos.esa.int/web/gaia/dpac/consortium>). Funding for the DPAC has been provided by national institutions, in particular the institutions participating in the *Gaia* Mul-

tilateral Agreement. We acknowledge the use of data provided by the Centre d'Analyse de Données Etendues (CADE), a service of IRAP-UPS/CNRS (<http://cade.irap.omp.eu>, Paradis et al. 2012).

References

- Andersen, K. J., Herman, D., Aurlien, R., et al. 2023, A&A, 675, A13
 Arendt, R. G., Odegard, N., Weiland, J. L., et al. 1998, ApJ, 508, 74
 Basyrov, A., Suur-Uski, A.-S., Colombo, L. P. L., et al. 2023, A&A, 675, A10
 Bennett, C. L., Fixsen, D. J., Hinshaw, G., et al. 1994, ApJ, 434, 587
 Bennett, C. L., Larson, D., Weiland, J. L., et al. 2013, ApJS, 208, 20
 BeyondPlanck Collaboration. 2023, A&A, 675, A1
 Bianchini, F. & Fabbian, G. 2022, Phys. Rev. D, 106, 063527
 BICEP2 Collaboration, Ade, P. A. R., Aikin, R. W., et al. 2014, ApJ, 792, 62
 Boggess, N. W., Mather, J. C., Weiss, R., et al. 1992, ApJ, 397, 420
 Brilenkov, M., Fornazier, K. S. F., Hergt, L. T., et al. 2023, A&A, 675, A4
 Carlstrom, J. E., Ade, P. A. R., Aird, K. A., et al. 2011, PASP, 123, 568
 Colombo, L. P. L., Eskilt, J. R., Paradiso, S., et al. 2023, A&A, 675, A11
 Dame, T. M., Hartmann, D., & Thaddeus, P. 2001, ApJ, 547, 792
 Delouis, J. M., Pagano, L., Mottet, S., Puget, J. L., & Vibert, L. 2019, A&A, 629, A38
 Dickinson, C., Davies, R. D., & Davis, R. J. 2003, MNRAS, 341, 369
 Draine, B. T. 2011, ApJ, 732, 100
 Dunkley, J., Spergel, D. N., Komatsu, E., et al. 2009, ApJ, 701, 1804
 Edenhofer, G., Zucker, C., Frank, P., et al. 2024, A&A, 685, A82
 Eriksen, H. K., O'Dwyer, I. J., Jewell, J. B., et al. 2004, ApJS, 155, 227
 Eriksen, H. K., O'Dwyer, I. J., Jewell, J. B., et al. 2004, Astrophys. J. Suppl., 155, 227
 Fixsen, D. J., Cheng, E. S., Cottingham, D. A., et al. 1994, ApJ, 420, 457
 Fixsen, D. J., Weiland, J. L., Brodd, S., et al. 1997, ApJ, 490, 482
 Fowler, J. W., Niemack, M. D., Dicker, S. R., et al. 2007, Appl. Opt., 46, 3444
 Fruchter, A. S. & Hook, R. N. 2002, Publications of the Astronomical Society of the Pacific, 114, 144
 Gaia Collaboration et al. 2016, A&A, 595, A1
 Gaia Collaboration et al. 2018, A&A, 616, A1
 Galloway, M., Andersen, K. J., Aurlien, R., et al. 2023, A&A, 675, A3
 Galloway, M., E., G., et al. 2024, A&A, in preparation [arXiv:20xx.xxxxx]
 Gardner, J. P., Mather, J. C., Clampin, M., et al. 2006, Space Sci. Rev., 123, 485
 Geman, S. & Geman, D. 1984, IEEE Trans. Pattern Anal. Mach. Intell., 6, 721
 Gerakakis, S., Brilenkov, M., Ieronymaki, M., et al. 2023, The Open Journal of Astrophysics, 6, 10
 Gjerløw, E., Ihle, H. T., Galeotta, S., et al. 2023, A&A, 675, A7
 Gjerløw et al. 2024a, A&A, in preparation [arXiv:20xx.xxxxx]
 Gjerløw et al. 2024b, A&A, in preparation [arXiv:20xx.xxxxx]
 Górski, K. M., Hivon, E., Banday, A. J., et al. 2005, ApJ, 622, 759
 Handley, W. J., Hobson, M. P., & Lasenby, A. N. 2015, MNRAS, 453, 4384
 Hauser, M. G., Arendt, R. G., Kelsall, T., et al. 1998, ApJ, 508, 25
 Hauser, M. G., Kelsall, T., Leisawitz, D., & Weiland, J. 1998, *COBE Diffuse Infrared Background Experiment (DIRBE) Explanatory Supplement*, version 2.3, NASA/GSFC, Greenbelt, MD
 Husser, T. O., Wende-von Berg, S., Dreizler, S., et al. 2013, A&A, 553, A6
 Ihle, H. T., Bersanelli, M., Franceschet, C., et al. 2023, A&A, 675, A6
 Johnson, H. L. 1966, ARA&A, 4, 193
 Keihänen, E. & Reinecke, M. 2012, A&A, 548, A110
 Keihänen, E., Suur-Uski, A.-S., Andersen, K. J., et al. 2023, A&A, 675, A2
 Kelsall, T., Weiland, J. L., Franz, B. A., et al. 1998, ApJ, 508, 44
 Leinert, C., Bowyer, S., Haikala, L. K., et al. 1998, A&AS, 127, 1
 Lenz, D., Doré, O., & Lagache, G. 2019, ApJ, 883, 75
 Lewis, A. & Bridle, S. 2002, Phys. Rev. D, 66, 103511
 Magner, T. J. 1987, Optical Engineering, 26, 264
 Maris, M., Burigana, C., & Fogliani, S. 2006, A&A, 452, 685
 Mather, J. C., Cheng, E. S., Cottingham, D. A., et al. 1994, ApJ, 420, 439
 Mather, J. C., Fixsen, D. J., Shafer, R. A., Mosier, C., & Wilkinson, D. T. 1999, ApJ, 512, 511
 McCarthy, F. 2024, arXiv e-prints, arXiv:2405.13470
 Millea, M., Anderes, E., & Wandelt, B. D. 2019, Phys. Rev. D, 100, 023509
 Murakami, H., Baba, H., Barthel, P., et al. 2007, PASJ, 59, S369
 Neugebauer, G., Habing, H. J., van Duinen, R., et al. 1984, ApJ, 278, L1
 Odegard, N., Weiland, J. L., Fixsen, D. J., et al. 2019, ApJ, 877, 40
 Paradis, D., Dobashi, K., Shimoikura, T., et al. 2012, A&A, 543, A103
 Paradiso, S., Colombo, L. P. L., Andersen, K. J., et al. 2023, A&A, 675, A12
 Partridge, R. B. & Peebles, P. J. E. 1967, ApJ, 148, 377
 Planck Collaboration XIV. 2014, A&A, 571, A14
 Planck Collaboration IX. 2016, A&A, 594, A9
 Planck Collaboration X. 2016, A&A, 594, A10
 Planck Collaboration I. 2020, A&A, 641, A1
 Planck Collaboration II. 2020, A&A, 641, A2
 Planck Collaboration III. 2020, A&A, 641, A3

- Planck Collaboration IV. 2018, *A&A*, 641, A4
Planck Collaboration VI. 2020, *A&A*, 641, A6
Planck Collaboration Int. XVII. 2014, *A&A*, 566, A55
Planck Collaboration Int. XLVIII. 2016, *A&A*, 596, A109
Planck Collaboration LVII. 2020, *A&A*, 643, A42
Prézeau, G. & Reinecke, M. 2010, *ApJS*, 190, 267
Reach, W. T., Franz, B. A., Weiland, J. L., et al. 1995, *Nature*, 374, 521
San, M., Herman, D., Erikstad, G. B., Galloway, M., & Watts, D. J. 2022, arXiv e-prints, arXiv:2205.12962
San, M. et al. 2024, *A&A*, in preparation [arXiv:2406.01491]
Seljebotn, D. S., Bærland, T., Eriksen, H. K., Mardal, K. A., & Wehus, I. K. 2019, *A&A*, 627, A98
Silverberg, R. F., Hauser, M. G., Boggess, N. W., et al. 1993, in *Society of Photo-Optical Instrumentation Engineers (SPIE) Conference Series*, Vol. 2019, *Infrared Spaceborne Remote Sensing*, ed. M. S. Scholl, 180–189
Soifer, B. T., Neugebauer, G., & Houck, J. R. 1987, *ARA&A*, 25, 187
Tegmark, M. 1997, *ApJ*, 480, L87
Torrado, J. & Lewis, A. 2021, *JCAP*, 05, 057
Watts, D. et al. 2024, *A&A*, in preparation [arXiv:2406.01491]
Watts, D. J., Basyrov, A., Eskilt, J. R., et al. 2023, *A&A*, 679, A143
Wright, E. L., Eisenhardt, P. R. M., Mainzer, A. K., et al. 2010, *AJ*, 140, 1868
Zonca, A., Singer, L., Lenz, D., et al. 2019, *Journal of Open Source Software*, 4, 1298